NASA CR-159829

CALCULATION OF OBLIQUE-SHOCK-WAVE LAMINAR-BOUNDARY-LAYER INTERACTION ON A FLAT PLATE

Uriel Goldberg
General Electric Company
Lynn, Massachusetts

and

Eli Reshotko
Case Western Reserve University
Cleveland, Ohio

Prepared for

NATIONAL AERONAUTICS AND SPACE ADMINISTRATION
Lewis Research Center
Cleveland, Ohio 44135

March 1980

Grant NGR-36-027-064

TABLE OF CONTENTS

I. INTRODUCTION

The present work is an attempt to find an analytic approach to the oblique shock wave - laminar boundary layer interaction problem. It is well known that when a shock wave impinges upon a stationary object in the flow, there results a complex interaction between the shock wave and the boundary layer on the object, in which the pressure rise can feed upstream along the object and the resulting interaction can, for certain flow conditions, lead to separation (see Fig. 1). The thickening of the boundary layer caused by this upstream influence disturbs the external flow and it is therefore impossible to compute the boundary layer independently of the changes in the outer flow caused by the shock. Some free interaction conditions must be established to link the two regions.

The present work attempts to find a solution in the case of a two-dimensional flow along a flat plate at zero incidence.

The earliest works in this field are experimental. These include the works of Ackeret, Feldmann and Rott [1], Liepmann, Dhawan and Roshko [2], Chapman, Kuehn and Larson [3] and Hakkinen, Greber, Trilling and Abarbanel [4]. Later investigators used integral boundary layer solutions coupled with an appropriate pressure law. These works are based on the theory of Crocco and Lees [5,6]. These methods did produce solutions that separated, reattached and met a downstream boundary condition of zero pressure gradient flow, but were limited

to a small range of Mach numbers, Reynolds numbers and wall temperatures.

Reyhner and Flugge-Lotz [7] carried the approach a step further by coupling a finite difference boundary layer solution with a Prandtl-Meyer pressure law and successfully obtained solutions that included a separated region and met the downstream boundary conditions dictated by a zero pressure gradient flow.

All the previous solutions rely on two basic factors:

1. Garvine [8] has shown that when a boundary layer is coupled to the inviscid stream, the problem assumes an elliptic character in that the upstream boundary conditions cannot be completely specified but rather that the correct solution is dependent on satisfying a downstream boundary condition.

2. Interacting boundary layer solutions exhibit a nodal behavior in that they tend to branch away from weak interaction solutions towards either separation or an expansive flow (see Fig. 2).

The advantage of the present work over the previous ones is in the improved treatment of reverse flow regions: the customary device of eliminating or modifying the time-like terms in the streamwise-momentum and energy equations in this region [7, 9, 13] has been eliminated by adding a time-like term to both sides of these equations in the backflow region, thereby avoiding the change of the basic nature of these equations, as called for by the previous methods.

The main advantage of using the method employed in the present work is that it provides a solution to a given case in a short time (usually about one minute of computer time using the UNIVAC 1110) as opposed to considerably longer time when a Navier-Stokes procedure is employed using present technology computers. This has a strong bearing on cost considerations, yet the accuracy of a solution as produced by the present method is good enough for engineering purposes.

The present effort assumes that the Prandtl-Meyer relation adequately represents the external flow and the free interaction condition between the boundary layer and this external flow is through coupling the two regions along the displacement thickness surface by a relation between the external flow turning angle and the stream-wise derivative of the displacement thickness. Implicit in this work is the assumption that the boundary layer equations are applicable throughout the computational regime, which excludes large separation bubbles, where the normal pressure gradient is no longer negligible.

There are three parameters which are of fundamental importance in this problem: the starting point of the interaction, the location of the idealized shock, and its strength. Knowledge of the latter two of these quantities does not permit the knowledge of the third, and hence iterative calculations must be performed to find the third parameter, namely, the starting point of the interaction. The

determination of this parameter is done through meeting the downstream boundary conditions, which are: (a) weak interaction far enough downstream of the shock impingement location; (b) a downstream pressure which is compatible with the one predicted from purely inviscid considerations. These two conditions necessitate the employment of two iteration parameters, such that only a unique combination of them yields the correct downstream conditions. Adopting a combination of the work of Reyhner and Flugge-Lotz [7] and of Dwoyer [9], the two iteration parameters employed in the present work are the starting point of the interaction (assuming knowledge of the shock impingement location) and the second derivative of the displacement thickness at the shock impingement point.

The boundary layer equations are solved by a linear implicit finite difference technique [10].

Special treatment is applied for the backflow region, consisting of adding a $(-2\rho u \frac{\partial u}{\partial x})$ term to both sides of the streamwise momentum equation and a $(-2c_p \rho u \frac{\partial T}{\partial x})$ term to both sides of the energy equation, such that diagonal dominance of the resulting tridiagonal matrix is assured. This method is more accurate than the one used by Reyhner and Flugge-Lotz [7] and later by Dwoyer [9], which consisted of replacing the time-like terms in the streamwise momentum and energy equations by one-tenth their absolute values. No such artificial terms appear in the present work. The stabilizing method employed here is based on the successive iterations performed on each downstream station, so that by the time a station is converged (i.e.,

the free interaction condition is met) the streamwise momentum and energy equations are restored to their correct form to within a small prescribed tolerance.

II. LIST OF SYMBOLS

a	speed of sound, $a = \sqrt{\gamma RT}$, $[\frac{m}{sec}]$
C	Chapman-Rubesin constant (eq. 21)
c_f	skin friction coefficient, $C_f = \frac{\tau_w}{(1/2)\rho_\infty u_\infty^2}$
c_p	specific heat at constant pressure, $[\frac{cal}{kg.°C}]$
c_v	specific heat at constant volume, $[\frac{cal}{kg.°C}]$
f	exponent in power law for the viscosity
g	exponent in power law for the thermal conductivity
G	function of γ used in Prandtl-Meyer calculation, $G = \sqrt{\frac{\gamma+1}{\gamma-1}}$
J,j	counter for mesh points in the x-wise direction
JD	J at the last computational station, $x = x_{downstream}$
K	counter for mesh points in the y-wise direction
K_1,K_2	coefficients in the x_o-iteration procedure
k	thermal conductivity $[\frac{cal}{m \cdot sec \cdot °C}]$; also counter for mesh points in the y-wise direction (will be clear according to context)
L	reference length, [m] ($L = x_o$)
M	Mach number
m	number used to divide ΔX to reduce mesh size in x-direction
p	pressure, $[\frac{N}{m^2}]$
P	nondimensional pressure, $P = \frac{p}{p_o}$
P_f	pressure at the downstream station
Pr	Prandtl number, $Pr = \frac{\mu_o c_p}{k_o}$

q heat flux $[\frac{cal}{m^2 \cdot sec}]$; also quotient in power series for ΔX in the case of variable mesh size (clear from context)

R gas constant, $[\frac{m \cdot N}{kg \cdot °C}]$

R_{e_x} Reynolds number based on x, $R_{e_x} = \frac{\rho_o u_o}{\mu_o} x$

t temperature, [°C]

T nondimensional temperature, $T = \frac{t}{t_o}$

$\tilde{T}$ temporary temperature vector used in backflow region calculation

$\hat{T}$ intermediate solution vector for the temperature at a streamwise station, improved by each iteration at that station

u streamwise velocity, $[\frac{m}{sec}]$

U nondimensional streamwise velocity, $U = \frac{u}{u_o}$

$\tilde{U}$ temporary streamwise velocity vector used in backflow region calculations

$\hat{U}$ intermediate solution vector for the streamwise velocity at a streamwise station, improved by each iteration at that station

v normal velocity, $[\frac{m}{sec}]$

V nondimensional normal velocity, $V = \frac{\rho_o v L}{\mu_o}$

x streamwise coordinate, [m]

X nondimensional streamwise coordinate, $X = \frac{\mu_o x}{\rho_o u_o L^2} = \frac{(\frac{x}{L})}{R_{e_L}}$

x_o streamwise location of the beginning of strong interaction

x_{sh} streamwise location of the idealized shock impingement on the plate

y normal coordinate, [m]

Y nondimensional normal coordinate, $Y = \frac{y}{L}$

Greek Symbols

β pressure gradient, $\beta = \frac{dP}{dX}$

γ specific heat ratio, $\gamma = \frac{c_p}{c_v}$ (= 1.405 for air)

δ boundary layer thickness, [m]

δ^* boundary layer displacement thickness, [m]

ΔX streamwise mesh size

ΔY normal mesh size

μ viscosity, $[\frac{kg}{m \cdot sec}]$

ν Prandtl-Meyer angle, [rad]

ϕ flow turning angle, [rad]

τ shear stress, $[\frac{N}{m^2}]$

ρ density, $[\frac{kg}{m^3}]$

ε tolerance

η nondimensional normal coordinate used for initial profiles, $\eta = \frac{y}{\delta}$

Subscripts

o	evaluated in the free stream at x_o
∞	evaluated at the outer edge of the boundary layer
a	adiabatic
c	a computed value (i.e., $\delta^{*''}_c$)
d,downstr.	evaluated at the last streamwise station
f	evaluated at a far downstream or final station
g	a guessed value (i.e., $\delta^{*''}_g$)
i	a value for an iterated quantity at the ith iteration
INV	a quantity evaluated through inviscid considerations (i.e., P_{INV})
initial	a quantity evaluated at the initial streamwise station
j	evaluated at the jth streamwise station for any k
k	evaluated at the kth normal station for any j
j,k	evaluated at the (j,k) mesh point
j_{x_o}	evaluated at the streamwise station corresponding to x_o
w, wall	evaluated at the wall
x	derivative with respect to x. Also, evaluated at x (clear from context)
x_o	evaluated at $x = x_o$
x_{sh}	evaluated at $x = x_{shock}$ (shock impingement point)

Superscripts

'	total derivative with respect to the appropriate independent variable
*	nondimensional quantity, used for ρ, k and μ
$\overline{}$	nondimensional quantity used for δ and δ^*

III. GOVERNING EQUATIONS

The flow field is divided into a boundary layer and an external flow. The external flow is handled as a Prandtl-Meyer edge condition for the boundary layer. Although the Prandtl-Meyer relation is isentropic and correct only for expansions, it can be used for weak compressions since the change in entropy is proportional to the cube of the pressure change through compression waves, and this is a very small quantity when proceeding from one station to the next while marching streamwise through the mesh points. The presence of the shock is compensated for by changing the reference Prandtl-Meyer angle when the computation procedure arrives one station downstream of the shock impingement point. The amount of change in the reference angle is automatically determined by the combined strength of the assumed shock and expansion fan and is corrected while the latter is iterated during the computational procedure.

Figure 1 shows the physical phenomenon treated by the computational procedure, indicating the important locations and geometrical features. x_o is the location where the compression waves first appear, and consequently where the pressure begins to rise from its upstream value.

This compression turns the flow away from the wall with subsequent separation possible. This is followed by the combination of an oblique shock and an expansion fan at x_{sh}. This is the location

where the boundary layer edge is most removed from the wall, and where the flow turns most sharply towards the wall. The distance between x_o and x_{sh} is the measure of the extent of upstream influence present; the stronger the shock the larger this distance, and hence the larger the resulting backflow region. Further downstream, a second set of compression waves turns the flow back parallel to the wall, followed by reattachment and gradual reversion back to a weak interaction region. Since the present work does not incorporate a normal momentum equation (and hence assumes mild flow deviations from the flat plate and constant pressure normal to it) only small separated regions can be treated by the present approach.

III.a Boundary Layer Equations

The basic equations for the compressible, steady, two dimensional boundary layer, assuming a constant Cp, are

$$\rho\left(u\frac{\partial u}{\partial x}+v\frac{\partial u}{\partial y}\right)=-\frac{dp}{dx}+\frac{\partial}{\partial y}\left(\mu\frac{\partial u}{\partial y}\right) \tag{1}$$

$$\frac{\partial(\rho u)}{\partial x}+\frac{\partial(\rho v)}{\partial y}=0 \tag{2}$$

$$\rho c_p\left(u\frac{\partial t}{\partial x}+v\frac{\partial t}{\partial y}\right)=u\frac{dp}{dx}+\frac{\partial}{\partial y}\left(k\frac{\partial t}{\partial y}\right)+\mu\left(\frac{\partial u}{\partial y}\right)^2 \tag{3}$$

A perfect gas is assumed, for which

$$p=\rho R t \tag{4}$$

Power-law relations are used for both the viscosity and the thermal conductivity:

$$\mu = \mu_o \left(\frac{t}{t_o}\right)^f \tag{5}$$

$$k = k_o \left(\frac{t}{t_o}\right)^g \tag{6}$$

where μ_o and k_o are respectively the viscosity and thermal conductivity at the reference temperature t_o. A value of 0.76 has been used for both f and g.

The boundary conditions are

$u(x,o) = 0$

$v(x,o) = 0$ (for impermeable wall)

$v(x,o) = v_w(x)$ (for suction)

$u(x,\infty) = u_\infty(x)$

$t(x,o) = t_w$ constant wall temperature case

$t(x,\infty) = t_\infty(x)$

or

$$-k \left.\frac{\partial t}{\partial y}\right|_{y=o} = q$$ constant wall heat flux case

$t(x,\infty) = t_\infty(x)$

where $u_\infty(x)$ and $t_\infty(x)$ are furnished by the solution of the inviscid outer flow, to be discussed later.

III.b Dimensionless Forms and Reference Quantities

The dimensionless variables employed in this work are chosen so as to achieve two goals: (a) creating flow variables that are most convenient for the finite difference procedure in which they are to be used; (b) creating as few parameters as possible, to maximize computational convenience.

With these in mind, the following dimensionless variables are employed:

$$U=\frac{u}{u_o},\ V=\frac{\rho_o v L}{\mu_o},\ T=\frac{t}{t_o},\ P=\frac{p}{p_o},\ \rho^*=\frac{\rho}{\rho_o},$$

$$k^*=\frac{k}{k_o},\ \mu^*=\frac{\mu}{\mu_o},\ X=\frac{x\mu_o}{\rho_o u_o L^2},\ Y=\frac{y}{L}$$

where all quantities with subscript o are evaluated in the free stream at x_o, the point where the strong interaction starts, and L is a reference length in the direction normal to the wall.

With these new variables, the dimensionless equations now become

$$\rho^*\left(U\frac{\partial U}{\partial X}+V\frac{\partial U}{\partial Y}\right)=-\frac{1}{\gamma M_o^2}\frac{dP}{dX}+\frac{\partial}{\partial Y}\left(\mu^*\frac{\partial U}{\partial Y}\right) \qquad (1a)$$

$$\frac{\partial(\rho^* U)}{\partial X}+\frac{\partial(\rho^* V)}{\partial Y}=0 \qquad (2a)$$

$$\rho^*\left(U\frac{\partial T}{\partial x}+V\frac{\partial T}{\partial y}\right)=\frac{\gamma-1}{\gamma}U\frac{dp}{dx}+\frac{1}{Pr}\frac{\partial}{\partial y}\left(k^*\frac{\partial T}{\partial y}\right)+$$

$$(\gamma-1)M_o^2\mu^*\left(\frac{\partial U}{\partial y}\right)^2 \qquad (3a)$$

$$P=\rho^* T \qquad (4a)$$

$$\mu^*=T^f \qquad (5a)$$

$$k^*=T^g \qquad (6a)$$

where the free-stream Mach number at x_o is

$$M_o=\frac{u_o}{\sqrt{\gamma R t_o}}$$

and the Prandtl number at the same location is

$$Pr=\frac{\mu_o C_p}{k_o}$$

The corresponding dimensionless Boundary Conditions are:

$$U(X,0) = 0$$

$$V(X,0) = \begin{cases} 0 & \text{(impermeable wall)} \\ V_w(X) & \text{(suction)} \end{cases}$$

$$U(X,\infty) = \frac{u_\infty(X)}{u_o} = U_\infty(X)$$

For constant wall temperature

$$T(X,0) = Tw$$

$$T(X,\infty) = \frac{t_\infty(X)}{t_o} = T_\infty(X)$$

while for constant heat flux q

$$-k^* \frac{\partial T}{\partial Y}\Big|_{y=0} = \frac{qL}{k_o t_o}$$

$$T(X, \infty) = T_\infty(X)$$

Note: In all subsequent equations the asterisk used to indicate dimensionless density (ρ^*), thermal conductivity (k^*) and dynamic viscosity (μ^*) will be dropped, with the understanding that these variables are dimensionless as defined above.

The following quantities are given in the free stream at $x = x_o$: M_o, ρ_o, μ_o, t_o and k_o. Based on these, the reference quantities are defined as follows:

Velocity: $u_o = M_o \sqrt{\gamma R t_o}$

Static pressure: $p_o = \rho_o R t_o$.

The reference length, L, is chosen as the distance from the leading edge of the plate to the location of the start of the strong interaction, namely

$$L = X_o$$

which leads to the following dimensionless coordinates:

$$X = \frac{X/X_o}{Re_{X_o}} \quad , \quad Y = \frac{y}{X_o}$$

where

$$Re_{x_o} = \frac{\rho_o u_o x_o}{\mu_o}$$

III.c Edge Conditions

The edge conditions necessary for the solution of the governing equations are calculated from the Prandtl-Meyer relation which is strictly valid only for isentropic expansions. However, the Prandtl-Meyer relation can be used for weak compressions since the change in entropy is proportional to the third power of the change in pressure for compression waves, and this entropy change is very small when proceeding from one mesh point to the next one while marching downstream during the computational procedure. This approach has been found also by previous authors to work reasonably [7,9,13]. The main difficulty in the solution of the governing equations (1 - 6), is that the pressure, p, is one of the unknowns, since in the case of a strong interaction the viscous and inviscid regions mutually affect each other and the pressure field is a result of this interaction. This is the basic difference between strong and weak interaction cases, since in the latter the pressure field is dictated by the inviscid flow, so it becomes a known variable as far as the viscous layer is concerned. In the present situation an additional equation is necessary which expresses the mutual determination of the pressure field by the viscous and inviscid regions. This is

done by coupling the two regions along the displacement surface (see Appendix A1) by the relation

$$\tan^{-1}\left(\frac{v_\infty}{u_\infty}\right) = \phi = \phi_w + \tan^{-1}\left(\frac{d\delta^*}{dx}\right) \tag{7}$$

where the index ∞ refers to the conditions at the outer edge of the boundary layer. ϕ is now used in the Prandtl-Meyer relation through the Prandtl-Meyer angle ν:

$$\nu = \nu_o - \phi \tag{8}$$

where

$$\nu = \sqrt{\frac{\gamma+1}{\gamma-1}}\tan^{-1}\sqrt{\frac{\gamma-1}{\gamma+1}\left(M_\infty^2-1\right)} - \tan^{-1}\sqrt{M_\infty^2-1} \tag{9}$$

and ν_o is the reference Prandtl-Meyer angle. The value of ν_o is that for M_o until one station downstream of the shock impingement point, where it assumes a new value that depends on P_f through the combination of incident shock strength and expansion fan such that it also guarantees continuity of pressure across the shock impingement location. This new value of ν_o is updated during the iterations performed on the shock strength plus expansion fan, as part of the computational procedure. Once equation (9) is solved for M_∞ (see Appendix B), the edge conditions may be evaluated as follows:

$$T_\infty = \frac{1+\frac{\gamma-1}{2}M_o^2}{1+\frac{\gamma-1}{2}M_\infty^2} \tag{10}$$

$$P_\infty = T_\infty^{\frac{\gamma}{\gamma-1}} \tag{11}$$

$$U_\infty = \frac{M_\infty}{M_{o1}}\sqrt{T_\infty} \tag{12}$$

$$\rho_\infty = \frac{P_\infty}{T_\infty} \tag{13}$$

and the pressure gradient

$$\frac{dP_\infty}{dX} = \frac{\gamma (M_\infty^2 - 1)^{1/2}\left[1 + \frac{\gamma-1}{2} M_o^2\right]^{\frac{\gamma}{\gamma-1}}}{\left\{\left[1 + \frac{\gamma-1}{\gamma+1}(M_\infty^2 - 1)\right]^{-1} - M_\infty^{-2}\right\}\left[1 + \frac{\gamma-1}{2} M_\infty^2\right]^{\frac{2\gamma}{\gamma-1}}} \cdot \frac{d\phi}{dX} \tag{14}$$

In equation (14) the term $\frac{d\phi}{dX}$ appears, which has the following value:

$$\frac{d\phi}{dX} = \frac{d\phi_{ur}}{dX} + \frac{Re_{x_o} X_o \frac{d^2\delta^*}{dX^2}}{1 + \left(\frac{d\delta^*}{dx}\right)^2} \tag{14a}$$

The first term on the R.H.S. vanishes for a flat plate. It should be noted that the second term contains both δ^* and x_o. Hence changes in both influence the computation of the edge flow parameters, independently of each other. This has a strong bearing on the method of iterations employed in the present work which is basically a double iteration loop where δ^* and x_o each change while the other is frozen in its latest value.

IV. METHOD OF SOLUTION

IV.a Difference Equations

The basic equations, eqns. 1a - 6a, will now be rewritten in finite difference form. A linear implicit form has been chosen, having the distinct advantage that all equations are linear in the various unknowns, thus at each step the momentum equation may be solved for the streamwise velocity values at the new station, followed by the energy equation yielding the values of the temperature at this new station, then the density is obtained from the equation of state, and based on these the continuity equation is solved to provide the normal velocity at the new station. Finally the viscosity and thermal conductivity are found and the procedure may be advanced one step downstream. Backward differencing is employed for the streamwise derivatives and central differencing is used for the normal derivatives in both the streamwise-momentum and the energy equations, while backward differencing is used in both directions in the continuity equation. The differencing for both the momentum and energy equations is correct to order $(\Delta Y)^2$ in the normal direction and to order ΔX in the streamwise direction, whereas for the continuity equation the differencing is correct to orders ΔY and ΔX. Since the truncation error is of second order in the streamwise direction, a relatively large number of mesh points has been employed, resulting in a fine mesh. The difference equations

to follow are stable for all mesh sizes so long as $U \geq 0$.

Finite difference formulation of the governing equations;

$$\rho_{j,k}\left[U_{j,k}\frac{U_{j+1,k}-U_{j,k}}{\Delta X}+V_{j,k}\frac{U_{j+1,k+1}-U_{j+1,k-1}}{2(\Delta Y)}\right]=-\frac{1}{\gamma M_\infty^2}\frac{P_{j+1}-P_j}{\Delta X}+$$

$$\mu_{j,k}\left[\frac{U_{j+1,k+1}-2U_{j+1,k}+U_{j+1,k-1}}{(\Delta Y)^2}\right]+\left[\frac{\mu_{j,k+1}-\mu_{j,k-1}}{2(\Delta Y)}\right]\left[\frac{U_{j+1,k+1}-U_{j+1,k-1}}{2(\Delta Y)}\right] \qquad (1b)$$

$$\frac{\rho_{j+1,k+1}U_{j+1,k+1}-\rho_{j,k+1}U_{j,k+1}}{\Delta X}+\frac{\rho_{j+1,k+1}V_{j+1,k+1}-\rho_{j+1,k}V_{j+1,k}}{\Delta Y}=0 \qquad (2b)$$

$$\rho_{j,k}\left[U_{j,k}\frac{T_{j+1,k}-T_{j,k}}{\Delta X}+V_{j,k}\frac{T_{j+1,k+1}-T_{j+1,k-1}}{2(\Delta Y)}\right]=\frac{\gamma-1}{\gamma}U_{j,k}\frac{P_{j+1}-P_j}{\Delta X}+$$

$$\frac{k_{j,k}}{P_r}\left[\frac{T_{j+1,k+1}-2T_{j+1,k}+T_{j+1,k-1}}{(\Delta Y)^2}\right]+\frac{1}{P_r}\left[\frac{k_{j,k+1}-k_{j,k-1}}{2(\Delta Y)}\right]\cdot$$

$$\cdot\left[\frac{T_{j+1,k+1}-T_{j+1,k-1}}{2(\Delta Y)}\right]+M_\infty^2(\gamma-1)\mu_{j,k}\left[\frac{U_{j+1,k+1}-U_{j+1,k-1}}{2(\Delta Y)}\right]^2 \qquad (3b)$$

$$\rho_{j+1,k}=\frac{P_{j+1}}{T_{j+1,k}} \qquad (4b)$$

$$\mu_{j+1,k}=\left(T_{j+1,k}\right)^f \qquad (5b)$$

$$k_{j+1,k}=\left(T_{j+1,k}\right)^g \qquad (6b)$$

IV.c Matrix Form of Equations

The momentum equation is rewritten in the form:

$$\left[\frac{-\rho_{j,k} V_{j,k}}{2(\Delta y)} - \frac{\mu_{j,k}}{(\Delta y)^2} + \frac{\mu_{j,k+1} - \mu_{j,k-1}}{4(\Delta y)^2}\right] U_{j+1,k-1} + \left[\frac{\rho_{j,k} U_{j,k}}{\Delta x} + 2\frac{\mu_{j,k}}{(\Delta y)^2}\right] U_{j+1,k} +$$

$$\left[\frac{\rho_{j,k} V_{j,k}}{2(\Delta y)} - \frac{\mu_{j,k}}{(\Delta y)^2} - \frac{\mu_{j,k+1} - \mu_{j,k-1}}{4(\Delta y)^2}\right] U_{j+1,k+1} = \frac{\rho_{j,k} U_{j,k}^2}{\Delta x} - \frac{1}{\gamma M_\infty^2} \frac{P_{j+1} - P_j}{\Delta x} \quad (1c)$$

This equation, written out for all k, assumes the form

$$\begin{bmatrix} \beta_1 & \Omega_1 & & & & & \\ \alpha_2 & \beta_2 & \Omega_2 & & & & \\ & \alpha_3 & \beta_3 & \Omega_3 & & & \\ & & - & - & - & & \\ & & & \alpha_k & \beta_k & \Omega_k & \\ & & & & - & - & - \\ & & & & & \alpha_{n-1} & \beta_{n-1} & \Omega_{n-1} \\ & & & & & & \alpha_n & \beta_n \end{bmatrix} \begin{Bmatrix} U_{j+1,1} \\ U_{j+1,2} \\ U_{j+1,3} \\ - \\ U_{j+1,k} \\ - \\ U_{j+1,n-1} \\ U_{j+1,n} \end{Bmatrix} = \begin{Bmatrix} \phi_1 \\ \phi_2 \\ \phi_3 \\ - \\ \phi_k \\ - \\ \phi_{n-1} \\ \phi_n - \Omega_n U_\infty \end{Bmatrix}$$

where

$$\alpha_k = -\frac{\rho_{j,k} V_{j,k}}{2(\Delta Y)} - \frac{\mu_{j,k}}{(\Delta Y)^2} + \frac{(\mu_{j,k+1} - \mu_{j,k-1})}{4(\Delta Y)^2}$$

$$\beta_k = \frac{\rho_{j,k} U_{j,k}}{\Delta X} + 2\frac{\mu_{j,k}}{(\Delta Y)^2}$$

$$\Omega_k = \frac{\rho_{j,k} V_{j,k}}{2(\Delta Y)} - \frac{\mu_{j,k}}{(\Delta Y)^2} - \frac{(\mu_{j,k+1} - \mu_{j,k-1})}{4(\Delta Y)^2}$$

$$\phi_k = \frac{\rho_{j,k} U_{j,k}^2}{\Delta X} - \frac{1}{\gamma M_\infty^2} \frac{P_{j+1} - P_j}{\Delta X}$$

This matrix equation is used to solve for $U_{j+1,k}$ using a tridiagonal matrix inversion technique.

The energy equation is written as:

$$\left[-\frac{\rho_{j,k} V_{j,k}}{2(\Delta Y)} - \frac{1}{P_r}\frac{k_{j,k}}{(\Delta Y)^2} + \frac{1}{P_r}\frac{(k_{j,k+1} - k_{j,k-1})}{4(\Delta Y)^2}\right] T_{j+1,k-1} +$$

$$\left[\frac{\rho_{j,k} U_{j,k}}{\Delta X} + \frac{2}{P_r}\frac{k_{j,k}}{(\Delta Y)^2}\right] T_{j+1,k} +$$

$$\left[\frac{\rho_{j,k} V_{j,k}}{2(\Delta Y)} - \frac{1}{P_r}\frac{k_{j,k}}{(\Delta Y)^2} - \frac{1}{P_r}\frac{(k_{j,k+1} - k_{j,k-1})}{4(\Delta Y)^2}\right] T_{j+1,k+1} =$$

$$\frac{\gamma-1}{\gamma} U_{j,k} \frac{P_{j+1} - P_j}{\Delta X} + (\gamma-1) M_\infty^2 \mu_{j,k} \left[\frac{U_{j+1,k+1} - U_{j+1,k-1}}{2(\Delta Y)}\right]^2 +$$

$$\rho_{j,k} U_{j,k} \frac{T_{j,k}}{\Delta X} \qquad (3c)$$

Written out for all k for the case of constant wall temperature, we get

$$\begin{bmatrix} \beta_1' & \Omega_1' & & & & & \\ \alpha_2' & \beta_2' & \Omega_2' & & & & \\ - & - & - & \cdots & & & \\ & \alpha_k' & \beta_k' & \Omega_k' & & & \\ & & - & - & - & & \\ & & & \alpha_{n-1}' & \beta_{n-1}' & \Omega_{n-1}' & \\ & & & & \alpha_n' & \beta_n' & \end{bmatrix} \begin{Bmatrix} T_{j+1,1} \\ T_{j+1,2} \\ - \\ T_{j+1,k} \\ - \\ T_{j+1,n-1} \\ T_{j+1,n} \end{Bmatrix} = \begin{Bmatrix} \phi_1' - \alpha_1' T_w \\ \phi_2' \\ - \\ \phi_k' \\ - \\ \phi_{n-1}' \\ \phi_n' - \Omega_n' T_\infty \end{Bmatrix}$$

where

$$\alpha_k' = -\frac{\rho_{j,k} V_{j,k}}{2(\Delta Y)} - \frac{1}{P_r}\frac{k_{j,k}}{(\Delta Y)^2} + \frac{1}{P_r}\frac{(k_{j,k+1} - k_{j,k-1})}{4(\Delta Y)^2}$$

$$\beta_k' = \frac{\rho_{j,k} U_{j,k}}{\Delta X} + \frac{2}{P_r}\frac{k_{j,k}}{(\Delta Y)^2}$$

$$\Omega_k' = \frac{\rho_{j,k} V_{j,k}}{2(\Delta Y)} - \frac{1}{P_r}\frac{k_{j,k}}{(\Delta Y)^2} - \frac{1}{P_r}\frac{(k_{j,k+1} - k_{j,k-1})}{4(\Delta Y)^2}$$

$$\phi_k' = \frac{\gamma-1}{\gamma} U_{j,k}\frac{P_{j+1} - P_j}{\Delta X} + (\gamma-1) M_\infty^2 \mu_{j,k}\left[\frac{U_{j+1,k+1} - U_{j+1,k-1}}{2(\Delta Y)}\right]^2 +$$

$$\rho_{j,k} U_{j,k}\frac{T_{j,k}}{\Delta X}$$

This is solved for $T_{j+1,k}$ using, again, a tridiagonal matrix inversion. Now we can find from the perfect gas law

$$\rho_{j+1,k} = \frac{P_{j+1}}{T_{j+1,k}} \tag{4b}$$

Next the continuity equation is solved to yield

$$V_{j+1,k+1} = \left(\frac{\rho_{j+1,k}}{\rho_{j+1,k+1}}\right) V_{j+1,k} + \frac{\Delta y}{\Delta x}\left[\left(\frac{\rho_{j,k+1}}{\rho_{j+1,k+1}}\right) U_{j,k+1} - U_{j+1,k+1}\right] \tag{2c}$$

This solution is started at the plate (y=0) where $V_{j+1,o} = 0$ (or $V_{j+1,o} = V_w(X)$) and marched out to the free stream. Finally, the viscosity and thermal conductivity for the (j+1)st station are computed:

$$\mu_{j+1,k} = (T_{j+1,k})^f \tag{5b}$$

$$k_{j+1,k} = (T_{j+1,k})^g \tag{6b}$$

This completes the solution for the (j+1) st station and the method is now applied to the next downstream station.

V. COMPUTATIONAL PROCEDURE

V.a Initial Profiles

The initial velocity profile is generated by an iterative procedure that is started with the Pohlhausen polynomial for the flat plate laminar boundary layer.

$$U_{initial} = 2\eta - 2\eta^3 + \eta^4 \tag{15}$$

where

$$\eta = \frac{y}{\delta_{initial}}$$

In terms of the Y-coordinate,

$$\eta = \frac{YX_o}{\delta_{initial}}$$

where $\delta_{initial}$ is tentatively taken at its Mach zero value

$$\delta_{initial} = 5.0\sqrt{\frac{\nu_o X_{initial}}{u_o}}$$

The initial station, $x_{initial}$, is the predetermined station where the computational procedure starts. Hence

$$U_{initial} = 2\left[\frac{YX_o}{\delta_{initial}} - \left(\frac{YX_o}{\delta_{initial}}\right)^3\right] + \left(\frac{YX_o}{\delta_{initial}}\right)^4 \tag{15a}$$

and in finite difference form

$$U_{1,k} = 2\left[\frac{X_o}{\delta_{initial}} k\Delta y - \left(\frac{X_o}{\delta_{initial}} k\Delta y\right)^3\right] + \left(\frac{X_o}{\delta_{initial}} k\Delta y\right)^4 \tag{15b}$$

with k going from zero up to k_{final}, corresponding to the last mesh point in the normal direction.

The initial representation of the temperature profile uses the Crocco relation between temperature and velocity for a flat plate with zero pressure gradient which is strictly valid only for Pr = 1:

$$T_{initial} = \frac{t_w}{t_o} + \left(1 - \frac{t_w}{t_o}\right) U_{initial} + \frac{\gamma - 1}{2} M_o^2 \, U_{initial} \left(1 - U_{initial}\right) \qquad (16)$$

which becomes, in finite difference form,

$$T_{i,k} = \frac{t_w}{t_o} + \left(1 - \frac{t_w}{t_o}\right) U_{i,k} + \frac{\gamma - 1}{2} M_o^2 \, U_{i,k} \left(1 - U_{i,k}\right) \qquad (16a)$$

Since these profiles do not correspond to the situation in the flow field ($M \neq 0$, $Pr \neq 1$) at our initial station, they are refined iteratively by using them to solve the equations of motion for one step downstream with zero pressure gradient, and then using the resulting profiles as new initial profiles. This procedure is repeated 10 times to ensure realistic initial profiles that are solutions to the difference equations and thereby allow smooth marching downstream from them.

V.b Treatment of Reversed Flow

The matrix U-equation was found to be

$$
\begin{bmatrix}
\beta_1 & \Omega_1 & & & & & \\
\alpha_2 & \beta_2 & \Omega_2 & & & & \\
 & \alpha_3 & \beta_3 & \Omega_3 & & & \\
 & & - & - & - & & \\
 & & & - & - & - & \\
 & & & & - & - & - \\
 & & & & & \alpha_{n-1} & \beta_{n-1} \quad \Omega_{n-1} \\
 & & & & & & \alpha_n \quad \beta_n
\end{bmatrix}
\begin{Bmatrix}
U_{j+1,1} \\ U_{j+1,2} \\ U_{j+1,3} \\ - \\ - \\ - \\ U_{j+1,n-1} \\ U_{j+1,n}
\end{Bmatrix}
=
\begin{Bmatrix}
\phi_1 \\ \phi_2 \\ \phi_3 \\ - \\ - \\ - \\ \phi_{n-1} \\ \phi_n - \Omega_n U_\infty
\end{Bmatrix}
$$

where

$$\alpha_k = -\frac{\rho_{j,k} V_{j,k}}{2(\Delta y)} - \frac{\mu_{j,k}}{(\Delta y)^2} + \frac{(\mu_{j,k+1} - \mu_{j,k-1})}{4(\Delta y)^2}$$

$$\beta_k = \frac{\rho_{j,k} U_{j,k}}{\Delta x} + 2\frac{\mu_{j,k}}{(\Delta y)^2} \qquad (17)$$

$$\Omega_k = \frac{\rho_{j,k} V_{j,k}}{2(\Delta y)} - \frac{\mu_{j,k}}{(\Delta y)^2} - \frac{(\mu_{j,k+1} - \mu_{j,k-1})}{4(\Delta y)^2}$$

$$\phi_k = \frac{\rho_{j,k} U_{j,k}^2}{\Delta x} - \frac{1}{\gamma M_\infty^2} \frac{P_{j+1} - P_j}{\Delta x} \qquad (18)$$

In order to maintain numerical stability of this tridiagonal equation, diagonal dominance (DD) must be preserved. This means that the following must be maintained:

$$\alpha_k + \beta_k + \Omega_k > 0$$

or

$$\frac{\rho_{j,k} U_{j,k}}{\Delta X} > 0$$

This shows that DD will be lost when $U_{j,k} \leq 0$, that is, in a reversed flow region (see Appendix A2).

In order to avoid this problem, the usual method employed by several authors (C.F. Ref. 7) is to drop the time-like term $\rho u \cdot u_x$ for $u \leq 0$, which provides marginal stability: $\alpha_k + \beta_k + \Omega_k = 0$, or, to assure that $\alpha_k + \beta_k + \Omega_k > 0$, the term $\rho u \cdot u_x$ is replaced by $0.1|\rho u| u_x$ wherever $\rho u < 0$. This means that the term $\frac{\rho_{j,k} U_{j,k}}{\Delta X}$ in the expression for β_k, eq. (17), is replaced by $\frac{0.1\rho_{j,k}|U_{j,k}|}{\Delta X}$. Physically this implies adding a small artificial convection term to the momentum equation. The claim usually made is that this creates only a small additional error as compared with that caused by the neglect of the $\rho u u_x$ term, and it guarantees DD. However, both of the above methods actually change the basic nature of the momentum equation in the backflow region, and this should be avoided.

The method employed in the present work is to add

$(-\frac{2\rho_{j,k}U_{j,k}}{\Delta X})U_{j+1,k}$ to <u>both</u> sides of the momentum equation, eqn. (1c), whenever $U_{j,k} < 0$. By doing so it is guaranteed that the momentum equation <u>remains unaltered</u> in the backflow region. There is a difficulty in doing this, however, since the term added to the R.H.S. of the equation in its matrix form, i.e., to ϕ_k, eqn. (18), contains the term $(U_{j+1,k})$, which is not known (the $\{U_{j+1,k}\}$ vector is the unknown of the matrix equation). This problem is solved by taking advantage of the fact that there are iterations performed at each J-station. Thus, a term $-\frac{2\rho_{j,k}U_{j,k}}{\Delta X}\tilde{U}_k$ is added to ϕ_k for $U_{j,k} < 0$, where $\tilde{U}_k$ is the solution $\hat{U}_{j+1,k}$ obtained from the previous iteration on the J+1st station. This term becomes closer and closer to the correct value, $U_{j+1,k}$, with each iteration, and by the time the last iteration on the J+1st station is reached, the following exists:

$$\left|1-\frac{\tilde{U}_k}{U_{j+1,k}}\right| < \varepsilon$$

and hence $\tilde{U}_k$ is within ε from $U_{j+1,k}$, thereby guaranteeing that the momentum equation at each J-station is correctly represented whether in the backflow region or not.

By employing this approach, the effective result is that the term $\frac{\rho_{j,k}U_{j,k}}{\Delta X}$ is replaced by $\frac{\rho_{j,k}|U_{j,k}|}{\Delta X}$ for $U_{j,k} < 0$, thereby guaranteeing DD, and yet no alteration of the momentum equation is caused as a consequence.

A similar situation holds for the energy equation:

The matrix form for the energy equation was found to be

$$\begin{bmatrix} \beta_1' & \Omega_1' & & & & & \\ \alpha_2' & \beta_2' & \Omega_2' & & & & \\ & \alpha_3' & \beta_3' & \Omega_3' & & & \\ & & - & - & - & & \\ & & & - & - & - & \\ & & & & - & - & - \\ & & & & & \alpha_{n-1}' & \beta_{n-1}' & \Omega_{n-1}' \\ & & & & & & \alpha_n' & \beta_n' \end{bmatrix} \begin{Bmatrix} T_{j+1,1} \\ T_{j+1,2} \\ T_{j+1,3} \\ - \\ - \\ - \\ T_{j+1,n-1} \\ T_{j+1,n} \end{Bmatrix} = \begin{Bmatrix} \phi_1' - \alpha_1' T_w \\ \phi_2' \\ \phi_3' \\ - \\ - \\ - \\ \phi_{n-1}' \\ \phi_n' - \Omega_n' T_\infty \end{Bmatrix}$$

where

$$\alpha_k' = -\frac{\rho_{j,k} V_{j,k}}{2(\Delta Y)} - \frac{1}{P_r}\frac{k_{j,k}}{(\Delta Y)^2} + \frac{1}{P_r}\frac{(k_{j,k+1} - k_{j,k-1})}{4(\Delta Y)^2}$$

$$\beta_k' = \frac{\rho_{j,k} U_{j,k}}{\Delta X} + \frac{2}{P_r}\frac{k_{j,k}}{(\Delta Y)^2} \qquad (19)$$

$$\Omega'_k = \frac{\rho_{j,k} V_{j,k}}{2(\Delta Y)} - \frac{1}{Pr} \frac{k_{j,k}}{(\Delta Y)^2} - \frac{1}{Pr} \frac{(k_{j,k+1} - k_{j,k-1})}{4(\Delta Y)^2}$$

$$\phi'_k = \frac{\gamma - 1}{\gamma} U_{j,k} \frac{P_{j+1} - P_j}{\Delta X} + (\gamma - 1) M_\infty^2 \mu_{j,k} \left[\frac{U_{j+1,k+1} - U_{j+1,k-1}}{2(\Delta Y)} \right]^2$$

$$+ \rho_{j,k} U_{j,k} \frac{T_{j,k}}{\Delta X} \qquad (20)$$

Again, to maintain DD it is necessary that

$$\alpha'_k + \beta'_k + \Omega'_k > 0$$

which means that the following must hold:

$$\frac{\rho_{j,k} U_{j,k}}{\Delta X} > 0$$

Hence the term $(-\frac{2\rho_{j,k}U_{j,k}}{\Delta X})T_{j+1,k}$ is added to both sides of the energy equation, eq. (3c), so as to keep the energy equation unchanged in the backflow region. This time a temporary $\tilde{T}_k$ vector is needed to multiply the above term when adding it to ϕ'_k, eq. (20). The solutions $\hat{T}_{J+1,k}$ of the successive iterations on each J station are used for this purpose, and by the time the last iteration is reached, station J+1 is converged and the relation

$$\left| 1 - \frac{\tilde{T}_k}{T_{j+1,k}} \right| < \varepsilon$$

is guaranteed, thereby keeping the energy equation unaltered in the backflow region and yet maintaining DD there.

V.c Iteration Logic

As can be seen from the Prandtl-Meyer equations employed in the

present work, eqs. 7 - 14a, the edge conditions are based on δ^* and its 1st and 2nd derivatives. Since δ^* is dependent on the velocity and density profiles, which are themselves dependent on the edge conditions, it is obvious that an iterative approach is necessary. Hence the computational procedure is as follows:

1. An initial guess is made for $\delta^{*''}$, denoted by $\delta^{*''}_g$.
2. This guess is integrated numerically to obtain $\delta^{*'}_g$. (See Appendix C1)
3. $\delta^{*''}_g$ and $\delta^{*'}_g$ are used to obtain the boundary layer edge conditions through the Prandtl-Meyer procedure, eqns. 7,8,9,14 and 14a.
4. The edge conditions are used to integrate the boundary layer equations at the new x-wise station.
5. From the new profiles, a value for δ^* is computed, denoted by δ^*_c.
6. δ^*_c is twice numerically differentiated to obtain $\delta^{*''}_c$. (See Appendix C2) Since a three-point backward differentiation is used here, a numerical problem exists at station $J_{x_{sh}} + 1$, where the procedure smoothes out the jump in δ^* that is induced at $J_{x_{sh}}$. This may account for the local instabilities which occurred at station $J_{x_{sh}} + 1$ and continued for a few stations downstream of it, as will be seen in the figures.
7. $\delta^{*''}_g$ and $\delta^{*''}_c$ are compared. If they do not agree to within a required tolerance, a new guess for $\delta^{*''}_g$ is made, using a Newton-Raphson procedure (see Appendix C3), and a return is made to step #2. When $\delta^{*''}_c$ and $\delta^{*''}_g$ agree to within the specified tolerance, the

present x-wise station is considered solved and the whole procedure is marched one step downstream, with the last $(\delta^{*"})_J$ used as the first guess for $\delta^{*"}$ at the J + 1st station.

The above procedure begins with the supplied initial profiles and marches downstream until no further changes in the pressure field occur, indicating that the shock wave-boundary layer interaction is over.

Two distinct cases may occur at the downstream region (i.e., far enough downstream for the effect of the shock to diminish);

a. the pressure does not acquire a steady value, but, rather, either goes rapidly to zero to increases rapidly;

b. the pressure has a steady value, which, however, is different from the one physically occurring (determined by the shock strength).

The present work employs two distinct procedures to correct these behaviors and to pick successively better branches.

In case (a), the branching solutions are controlled by fixing $\delta^{*"}$ at the station corresponding to the shock impingement location, $J_{x_{sh}}$ (see Appendix D). The perturbation in $\delta^{*"}$ is created by using the value at the last station before $J_{x_{sh}}$, multiplied by a parameter called PARDEL. This in effect means introducing a pressure gradient discontinuously at this station, thereby triggering a branch. The successive values for $\delta^{*"}$ (through PARDEL) are determined by a Newton-Raphson procedure such that the correct $\delta^{*"}_{j_{x_{sh}}}$ leads the computational procedure to a level branch, i.e., constant pressure at

the downstream weak interaction region (see Appendix C4). Figure 2 shows the effect of $\delta^{*''}_{j_{x_{sh}}}$ on the branching behavior. Along with this branch control, ν_o is also changed at $J_{x_{sh}} + 1$ to keep a constant pressure across $J_{x_{sh}}$, where the shock and accompanying expansion fan are located. The iteration procedure described above (steps 1 - 7) is not performed at station $J_{x_{sh}}$ to keep the discontinuity in pressure gradient introduced by PARDEL.

In case (b), the branching solutions are controlled by fixing a new value for x_o (see Appendix D). The closer x_o is to the point where the ideal shock impinges on the boundary layer, (x_{sh}), the weaker the resulting interaction and the weaker P_f, while the further x_o is upstream of the shock impingement point, the stronger the resulting interaction and the stronger P_f, Hence too compressive branches are corrected by moving x_o downstream, closer to x_{sh}, while too expansive branches are corrected by moving x_o upstream, further away from x_{sh} (see Appendix E). Changing x_o changes Re_{x_o}, of course. Figure 3 shows the effect of x_o on the branching behavior, indicating that minute changes in x_o suffice to impose a large change in P_f. This behavior has been indicated also by Reyhner and Flugge-Lotz [7]. While an x_o iteration is performed, $\delta^{*''}_{j_{x_{sh}}}$ is frozen at its latest value, and vice versa. Usually only a few $\delta^{*''}_{x_{sh}}$-type of iterations are necessary to obtain a steady downstream pressure. Once this is attained, all further iterations are of the x_o-type, with $\delta^{*''}_{x_{sh}}$ frozen at its latest value.

The accompanying flow chart (Fig. 4), explains the computational procedure, and Fig. 5 shows how $\delta^{*''}_{g}$ varies with x. This figure shows regions of both strong and weak interaction within the same case. For the weak interaction it is possible to use the relation for the displacement thickness in the case of a compressible laminar flat-plate flow with Pr = 0.72 [20] as a check on the numerical results:

$$\frac{\delta^*}{x}\sqrt{Re_x} = \sqrt{C}\left[1.7208 + 1.9384\left(\frac{t_w}{t_\infty} - 1\right) + 0.2878(\gamma-1)M_\infty^2\right] \tag{21}$$

where C is the Chapman-Rubesin constant $C = \frac{\rho_w \mu_w}{\rho_\infty \mu_\infty}$ which is unity in our case, since $T_w = 1.0$.

Inserting numerical values into equation (21) and using the fact that $\frac{t_w}{t_\infty} = 1$, yields, for the particular $Re_{x_{sh}}$ of Fig. 5 (in dimensional form - all lengths in meters):

$$\delta^* = 8.5497 \times 10^{-4}\sqrt{x} \tag{22}$$

and

$$\frac{d^2\delta^*}{dx^2} = -2.1374 \times 10^{-4} x^{-3/2} \tag{23}$$

and, with

$$x = (J-1)\Delta x$$

equation (23) becomes

$$\frac{d^2\delta^*}{dx^2} = -52.4047\,(J-1)^{-3/2} \tag{24}$$

where the numerical value of Δx for the particular case of Fig. 5 has been used.

It is observed that the strong interaction case sharply deviates from the weak one between J = 60 and J = 150. The oscillatory behavior between J = 60 and J = 85 is attributed to the inherent numerical instability that results from numerical differentiation. As may be observed in Fig. 12 the boundary layer thickness (and hence also δ^*) exhibits a mild oscillatory behavior over the region corresponding roughly to $60 < J < 85$. (Emphasized by heavy dots.) When such a curve is twice numerically differentiated, the result may lead to unstable oscillations, since the nature of differentiation is to amplify any existing instability.

However, the iterative procedure used in the algorithm always managed to stabilize the computations based on $\delta^{*\prime\prime}$ since the effect of the iterative procedure is to produce an average trend line of $\delta^{*\prime\prime}$ in the oscillatory region. Downstream of J_{x_o}, $\delta^{*\prime\prime} > 0$ (disregarding a few isolated points where $\delta^{*\prime\prime} < 0$ as a result of local numerical instabilities downstream of $J_{x_{sh}}$, where reattachment occurs), which is characteristic of strong interactions (see also Fig. 19). Around J = 115 the strong interaction begins to decay and approaches the downstream weak interaction region asymptotically.

VI. COMPUTED RESULTS

Several examples have been run to test the method used in the present work. Common to these examples are the following flow parameters: $M_o = 2.0$, $T_w = 1.0$, $Pr = 0.70$, and $Re_{sh} = 3.89 \times 10^5$, corresponding to an altitude of 16,500 meters. The only parameter that was varied from one case to the next was the overall pressure ratio, P_f, which in effect, selected the shock strength. Examples have also been run with an adiabatic wall ($T_w = 1.67$) but became unstable for shock strengths corresponding to $P_f \geq 1.025$.

All computations were initiated at $\frac{x_{initial}}{x_{sh}} = 0.50$, with constant step sizes in both X and Y directions, the magnitudes of which changed during the execution of the program according to the current value of x_o, such that the final step sizes were determined by that x_o which produced the correct branching solution. The mesh size consisted of 200 points in the streamwise direction and 72 points in the normal direction. Increasing the number of points above 200 in the streamwise direction did not produce any change in the computed results.

Figure 6 shows the development of the streamwise velocity profiles over the flat plate. The separation develops smoothly but the reattachment is abrupt, with the first reattached profile exhibiting a reduced velocity region in the upper part of the subsonic section of the boundary layer (refer to corresponding profile

in Fig. 8). Since this is the profile immediately downstream of shock impingement, the reason for its shape is perhaps the local favorable pressure gradient that occurs at this location (Fig. 13), which in turn may be the result of the numerical calculation of $\delta_c^{*''}$ that smoothes out the jump in $\frac{dP}{dX}$ at $J_{x_{sh}}$. The profiles further downstream do not exhibit this bulge but their shape, possessing an inflection point, indicates a gradual recovery from this profile. The fourth profile after reattachment exhibits a small reversed flow near the wall. This tendency of an attached flow to re-separate has been observed also by Reyhner and Flugge-Lotz [7] and attributed to the combination of the Prandtl-Meyer relation and the assumption $\frac{\partial P}{\partial Y} = 0$, both of which are deficient in the reattachment zone. The method used here to eliminate this problem was to replace eqn. (14) beyond reattachment by a simple backward difference, $\frac{dP_\infty}{dX} = \frac{P_{j+1} - P_j}{\Delta X}$. Figure 6a is an enlarged detail of Fig. 6, showing the separation region.

Figure 7 is a comparison of streamwise velocity profiles for the cases of incipient separation ($P_f \tilde{=} 1.12$) and of a separated region ($P_f = 1.31$). It is observed that the thickening of the boundary layer is considerably more pronounced in the case of the separated region, as expected for a stronger interaction (stronger shock).

Figure 8 shows the development of the Mach number profiles for

P_f = 1.31. It is observed that the subsonic part of the boundary layer is roughly its inner 30% upstream of the shock impingement region and this changes to approximately the inner 40% of the boundary layer thickness downstream of this region. As the shock impingement region is approached, the subsonic layer increases up to about half of the boundary layer thickness, and decreases again after the shock impingement (see also Fig. 12).

Figure 9 shows the behavior of the normal velocity profiles. It will be observed that a part of the strong interaction region, starting at J=82 may be subdivided into five regions:

Region I : $82 \leq J \leq 90$, with negative normal edge velocity;
Region II : $91 \leq J \leq 97$, with positive normal edge velocity;
Region III : $98 \leq J \leq 101$, with strong negative edge velocity;
Region IV : $102 \leq J \leq 109$, with strong positive edge velocity;
Region V : $J \geq 110$, with negative edge velocity, gradually diminishing to zero.

The behavior in Region II is a consequence of the flow over the separated region, which has a component directed away from the wall. The behavior in Region III stems from the rather sharp velocity component directed towards the wall at the region of reattachment, while the behavior in Region IV is a result of the sharp turning of the flow away from the wall so as to become parallel to it downstream of reattachment. No explanation has been found for Regions I and V, except that the gradual diminishing of normal velocity in Region V is a demonstration of the slow switch to weak interaction, as can clearly be seen in Fig. 5. Since the strong interaction region is noted for its high irregularities (Fig. 5) and since the

normal velocity calculation is very sensitive to these irregularities, it is not helpful to analyze the normal velocity profiles in great detail.

Figure 10 shows the development of the static temperature profiles in the case of a cooled wall. The dissipation in the boundary layer causes a rise in the temperature, which is then reduced near the wall by the cooling ($T_w = 1.0$).

Figure 11 shows the development of the stagnation temperature profiles. The reduction in stagnation temperature through the boundary layer is caused by the conduction of heat from the boundary layer into the wall (cooled wall case). It is observed that the reduction in stagnation temperature is less in the separated region than in the attached regions indicating a lower heat transfer rate for the separated region than for the attached flows.

Figure 12 shows the development of the stagnation pressure profiles. The decrease in stagnation pressure is due to reduced velocity in the boundary layer. Note that the decrease is sharp in the supersonic part of the boundary layer and becomes smaller and smaller through the subsonic layer, until, at the immediate vicinity of the wall the stagnation pressure approaches the local static pressure. In the separated region, because of the small recirculation velocities, the stagnation pressure retains nearly its wall value further into the flow. Also indicated in Fig. 12 is the behavior of the boundary layer thickness over the plate (dotted). The most upstream part behaves in the manner of a flat plate profile. The

boundary layer thickness then shows a moderate increase downstream of x_o becoming sharper as the shock impingement location is approached and attaining a peak in the vicinity of shock impingement. Downstream of reattachment there is a rather sharp decrease in boundary layer thickness, forming the well known "neck", and further downstream a flat-plate-type of profile is attained again, indicating transition from strong to weak interaction (see also Fig. 19). The heavily dotted points indicate the regions where the boundary layer thickness profile wiggles the most (as a result of numerical instabilities) and the region downstream of x_o is causing the oscillatory behavior of δ^*" at that zone (see Fig. 5). For comparison, a compressible boundary layer thickness profile on a flat plate has also been included (dashed line). The computed thicknesses are slightly below the theoretical, but close enough so that the computed thicknesses are credible.

Figure 13 shows a typical static pressure profile over the plate, as produced by the program. It starts with a constant value corresponding to the upstream boundary conditions, followed by a relatively moderate increase starting at x_o. This continues until a short plateau is attained downstream of the point where the shock impinges. At the second compression region an abrupt jump in pressure occurs, followed by a constant value all the way downstream, corresponding to the downstream boundary conditions. The bulge seen immediately before the plateau is a result of slight

pressure drop just downstream of shock impingement and occured in almost every case in the present work. This pressure drop is perhaps due to the local numerical instability introduced by $\delta_c^{*''}$ at $J_{x_{sh}} + 1$, that smoothes out the jump in $\frac{dP}{dX}\Big|_{j_{x_{sh}}}$, and may be the reason behind the shape of the first reattached profile (see Fig. 6).

Figure 14 shoes a typical skin friction profile over the flat plate, as produced by the present program. The initial flat plate-type of behavior gives way, starting at x_o, to a rather sharp decrease in C_f leading to separation, followed subsequently by reattachment, and further downstream the profile again attains a flat plate-like shape. The wiggles in the separated region are due to local numerical instabilities (associated perhaps with the treatment of backflow regions) that plagued all cases which did not incorporate suction. (However, see Fig. 17.) This shape for the C_f profile in the separated region has been obtained also by Reyhner and Flugge-Lotz ([7], Fig. 15), including, particularly, the relatively large negative peak immediately prior to reattachment. The large positive bulge after reattachment is a direct consequence ofthe shape of the first reattached profile near the wall. As may be seen in Fig. 6, this profile has a large slope at the wall, causing the observed overshoot in C_f, This bulge dies out further downstream as the profile asymptotically attains its flat-plate value.

Figure 15 shows the original C_f profile for the case $P_f = 1.31$ and a "corrected" version where the positive bulge produced by the local numerical disturbance (Figs. 6,13) has been removed. The dashed

line indicates this region. As may be seen by comparison with Fig. 21, the shape of this profile agrees qualitatively with experimental data.

Figure 16 shows two skin friction profiles, one corresponding to a case approaching incipient separation, the other to that of a slightly separated region. It is observed that in the former case x_o is much closer to x_{sh} than in the latter case, indicating a weaker interaction. The bulge that occured in the lower figure at the reattachment region (substituted by a dashed line) did not occur in the weaker case, indicating that the local numerical disturbance which apparently produces the bulges (Figs. 6,13,14), is associated only with those cases that involve a strong enough interaction to induce separation.

Figure 17 shows the behavior of C_f over the plate with constant suction velocity of approximately 5% of the normal velocity at the boundary layer edge. This suction is applied at the indicated region, starting at x_o and ending slightly downstream of the shock impingement point. It is observed that all the numerical instabilities at the separated region have disappeared, resulting in a smooth profile. The separated region itself is smaller than for a similar case without suction (Fig. 14). The usual positive bulge at the reattachment region has also disappeared

Figure 18 shows plots of pressure and skin friction over the plate for the case $P_f = 1.31$. It is observed that the region

of sharply decreasing C_f coincides with the region of pressure rise downstream of x_o. The upper part of this rise together with the slight pressure plateau and the first part of the sharp rise in pressure occur over the separated region ($C_f < 0$) and further downstream both curves approach a constant downstream velue.

Figure 19 is a plot of a typical streamwise distribution of boundary layer thickness over the plate, starting at x_o. There is a sharp increase in thickness until a peak is reached at the shock impingement point, followed by a sharp decrease that forms the well known "neck", with a subsequent gradual increase, forming a flat-plate-like shape further downstream. (See also Fig. 12.) Note that at the shock impingement point the boundary layer is 50% thicker than at x_o. Note also that the curve is concave upward through $x \tilde{=} 1.19\ x_{sh}$, which explains why $\delta^{*''} > 0$ in the strong interaction region.

VII. COMPARISON WITH EXPERIMENTS

The experimental work of Hakkinen, Greber, Trilling and Abarbanel [4] has been used here for the purpose of comparison with the present numerical work. The experiments were conducted with an insulated wall, whereas the theory is for a cooled wall.

Figure 20 shows the result of a pressure profile comparison. It is observed that the pressure rise starting at x_o is slightly sharper than the one predicted by the present analysis. Furthermore, the pressure plateau is better defined than the present work predicts. Also, the second rise in pressure downstream of the shock impingement point, while exhibiting the same behavior, is predicted somewhat upstream of the place indicated by experiment. Lastly, while the program predicts a rather abrupt rise to the downstream pressure, the experiment indicates a more gradual behavior. All in all, the comparison shows a reasonably good fit between theory and experiment despite the mismatch in wall temperature.

Figure 21 compares skin friction profiles. It is seen that the decrease in C_f towards separation is more gradual than predicted by the program, and, while the point of separation is almost the same, the present work predicts a smaller separated region than indicated by experiment. Both these predictions, i.e., higher C_f with more rapid drop-off prior to separation and reduced separated region in comparison with experimental data, have been found also by

Dwoyer [9]. Downstream of reattachment the large discrepancy between the present work and experiment is due to the large positive bulge that is caused by the local numerical disturbance at the first reattached streamwise station. In summary, the present work compares quite favorably with experiment through separation.

VIII. CONCLUSIONS

The present work indicates that using the compressible boundary-layer equations coupled with an exterior Prandtl-Meyer flow does lead to an approximate solution to the problem of oblique shock wave-laminar boundary layer interaction.

The agreement with experiments, although not completely satisfactory, is nevertheless remarkable in light of the theoretical and numerical difficulties involved in the use of parabolic equations for the solution of an elliptic problem.

It is noted that the application of a relatively small amount of suction in the shock impingement region significantly reduces the size of the backflow region. Introducing suction into the calculation also proved to be especially helpful in reducing the severity of the numerical instabilities.

The use of a linear finite difference approach in the present work, while significantly simplifying the formulation of the equations and reducing computing time, might have nevertheless been part of the reason behind the local numerical instabilities that occured in critical locations in the strong interaction region. Employing a non-linear Crank-Nicholson method for the finite differences might have reduced or even eliminated these instabilities, and might have also permitted a reduction in the number of mesh points used in the streamwise direction.

The numerical differentiation procedure for $\delta_c^{*''}$, when performed at the first station downstream of shock impingement, is most probably responsible for the local numerical instabilities that occured at the region downstream of shock impingement. A practical way to eliminate this problemwould be to skip the iteration procedure on the $(J_{x_{sh}} + 1)$ station (in addition to $J_{x_{sh}}$ itself) and resume it at the $(J_{x_{sh}} + 2)$ station.

In summary, the present work does produce a gross picture for the behavior of the flow as a result of an oblique shock-laminar boundary layer interaction on a flat plate, especially for the pressure and skin friction distributions. However, the present work comes short of providing a reliable detailed picture of the flow in the strong interaction region.

IX. REFERENCES

1. Ackeret, J., Feldmann, F., and Rott, N., "Investigations of Compression Shocks and Boundary Layers in Gases Moving at High Speed", NACA Tech. Memor. 1113, Jan. 1957.

2. Liepmann, H.W., Roshko, A. and Dhawan, S., "On Reflection of Shock Waves from Boundary Layers", NACA Report 1100, 1952.

3. Chapman, D.R., Kuehn, D.M. and Larson, H.K., "Investigation of Separated Flows in Supersonic and Subsonic Streams with Emphasis on the Effect of Transition", NACA Report 1356, 1958.

4. Hakkinen, R.J., Greber, I., Trilling, L. and Abarbanel, S.S., "The Interaction of an Oblique Shock Wave with a Laminar Boundary Layer", NASA Memor, 2-18-59W, 1959.

5. Crocco, L. and Lees, L., "A Mixing Theory for the Interaction Between Dissipative Flows and Nearly Isentropic Streams", J. Aerospace Sci., 19, pp. 649-676, 1952.

6. Lees, L. and Reeves, B.L., "Supersonic Separated and Reattaching Laminar Flows: I. General Theory and Application to Adiabatic Boundary-Layer/Shock-Wave Interactions", AIAA Journal, Vol. 2, No. 11, pp. 1907-1920, 1964.

7. Reyhner, T.A. and Flugge-Lotz, I., "The Interaction of a Shock Wave with a Laminar Boundary Layer", Int. Journal of Nonlinear Mechanics, Vol. 3, pp. 173-199, 1966.

8. Garvine, R.W., "Upstream Influence in Viscous Interaction Problems", The Physics of Fluids, Vol. 11, No. 7, pp. 1413-1423, 1968.

9. Dwoyer, D.L., "Supersonic and Hypersonic Two-Dimensional Laminar Flow Over a Compression Corner", AIAA Comp. Fluid Dynamics Conference, pp. 69-83, 1973.

10. Hornbeck, R.W., "Numerical Marching Techniques for Fluid Flows with Heat Transfer", NASA SP-297, pp. 21-29, 1973.

11. Schlichting, H., "Boundary Layer Theory", 6th edition, McGraw-Hill, 1968.

12. Ames Research Staff, "Equations, Tables, and Charts for Compressible Flow", NACA Rep. 1135, 1953.

13. Levy, R., Shamroth, S.J. and McDonald, H., "Drag of Aircraft and Missiles-Interim Technical Report", United Technologies Research Center, 1976.

14. Hankey, W.L., Dwoyer, D.L. and Werle, M.J., "Branching Solutions for Supersonic Interacting Boundary Layers", AIAA Journal, Vol. 11, No. 9, pp. 1349-1351, 1973.

15. Werle, M.J., Dwoyer, D.L. and Hankey, W.L., "Initial Conditions for the Hypersonic-Shock/Boundary-Layer Interaction Problem", AIAA Journal, Vol. 11, No. 4, pp. 525-530, 1973.

16. Rose, W.C., "A Method for Analyzing the Interaction of an Oblique Shock Wave and a Boundary Layer", NASA SP-228, pp. 541-564, 1969.

17. Murphy, J.D., "A Critical Evaluation of Analytic Methods for Predicting Laminar-Boundary-Layer Shock-Wave Interaction", NASA SP-228, pp. 515-537, 1969.

18. Werle, M.J. and Vatsa, V.N., "New Method for Supersonic Boundary-Layer Separations", AIAA Journal, pp. 1491-1497, Nov. 1974.

19. Moses, H.L., Jones, R.R., O'Brien, W.F. and Peterson, R.S., "Simultaneous Solution of the Boundary Layer and Freestream with Separated Flow", AIAA Journal, Vol. 16, No. 1, pp. 61-66, 1978.

20. Low, G.M., "The Compressible Laminar Boundary Layer with Fluid Injection", NACA TN-3404, 1955.

APPENDIX A

BASIC DEFINITIONS FOR QUANTITIES USED IN THE PROGRAM

1. Displacement thickness:

$$\delta_j^* = \left[\int_0^\infty \left(1 - \frac{\rho u}{\rho_\infty u_\infty}\right) dy \right]_j \tag{A1}$$

where u_∞ is the x-velocity component obtained from an inviscid solution of the flow field and evaluated at the wall. Likewise for ρ_∞.

In the program a Simpson's Rule is used for the integration and the upper limit is determined by the simultaneous satisfaction of the following two requirements:

$$\begin{cases} \frac{\partial U_j}{\partial Y} < \varepsilon \\ \frac{\partial T_j}{\partial Y} < \varepsilon \end{cases}$$

where ε is a prescribed tolerance. This determines the edge of the boundary layer for each x-wise station.

2. Skin friction coefficient and the criterion for reversed flow:

$$C_f = \frac{\tau_w}{\frac{1}{2}\rho_\infty u_\infty^2} = \frac{\left[\mu\left(\frac{\partial u}{\partial y}\right)\right]_{y=0}}{\frac{1}{2}\rho_\infty u_\infty^2} \tag{A2}$$

Hence the condition $C_{f_j} < 0$, indicating backflow, is determined as follows:

$$\left.\frac{\partial U}{\partial Y}\right|_{Y=0} \cong \frac{U_{j,1} - U_{j,0}}{\Delta Y}$$

so that $C_{f_j} < 0$ is equivalent to

$$\frac{2\mu_{j,0} U_{j,1}}{Re_{x_0} \rho_\infty U_\infty^2 \Delta Y} < 0$$

or

$$U_{j,1} < 0$$

APPENDIX B

NEWTON-RAPHSON PROCEDURE FOR THE PRANDTL-MEYER EQUATION

The general Newton-Raphson equation is:

$$X_{i+1} = X_i - \frac{f(X_i)}{f'(X_i)} \tag{B1}$$

In our case,

$$f(X) = G\tan^{-1}\left(\frac{\sqrt{X^2-1}}{G}\right) - \tan^{-1}\sqrt{X^2-1} + \phi - \nu_0 \tag{B2}$$

and

$$f'(X) = \frac{X}{\sqrt{X^2-1}}\left(\frac{1}{1+\frac{X^2-1}{G^2}} - \frac{1}{X^2}\right) + \frac{d\phi}{dX} \tag{B3}$$

where

$$G = \sqrt{\frac{\gamma+1}{\gamma-1}}$$

Now

$$\delta^* = L\int_0^{\bar{\delta}}\left(1-\frac{\rho U}{\rho_\infty U_\infty}\right)dY = L\int_0^{\bar{\delta}}\left(1-\frac{\rho U}{\rho_\infty M_\infty a_\infty}\right)dY$$

$$= L\left[\bar{\delta} - \int_0^{\bar{\delta}}\frac{\rho U}{\rho_\infty U_\infty}\,dY\right] \tag{B4}$$

$$\frac{d\delta^*}{dM_\infty} = L\int_0^{\bar{\delta}}\frac{\rho U}{\rho_\infty M_\infty U_\infty}\,dY = \frac{L}{M_\infty}\int_0^{\bar{\delta}}\frac{\rho U}{\rho_\infty U_\infty}\,dY$$

$$= \frac{L\bar{\delta} - \delta^*}{M_\infty} = \frac{\delta - \delta^*}{M_\infty} \tag{B5}$$

and hence

$$\frac{d^2\delta^*}{dx\,dM_\infty} = \frac{M_\infty\left(\frac{d\delta}{dx} - \frac{d\delta^*}{dx}\right) - (\delta - \delta^*)\frac{dM_\infty}{dx}}{M_\infty^2} \qquad \text{(B6)}$$

Order of magnitude analysis for the terms in Eqn. (B3):

$X = 2.$ (i.e., $M_\infty = 2$):

$$\frac{X/\sqrt{X^2-1}}{1+(X^2-1)/G^2} = 0.77$$

$$\frac{1}{X\sqrt{X^2-1}} = 0.29$$

For a flat plate

$$\frac{d\delta}{dx} \cong \frac{2.5}{\sqrt{Re_x}}$$

$$\frac{d\delta^*}{dx} \cong \frac{0.86}{\sqrt{Re_x}}$$

$$\therefore \frac{d\delta}{dx} - \frac{d\delta^*}{dx} \cong \frac{1.64}{\sqrt{Re_x}}$$

Also

$$\delta - \delta^* \cong 3.28\frac{X}{\sqrt{Re_x}}$$

and

$$\frac{\frac{dM_\infty}{dx}}{M_\infty^2} = O(1)$$

Hence

$$\frac{d^2\delta^*}{dx\,dM_\infty} = O\left(\frac{1}{\sqrt{Re_x}}\right)$$

Away from the immediate vicinity of x = 0 this term is negligible in comparison with the other two terms in eqn. (B3). Hence $\frac{d\phi}{dM_\infty}$ is negligible, noting that

$$\frac{d\phi}{dM_\infty} = \left[\frac{1}{1+(\delta^{*\prime})^2}\right]\frac{d^2\delta^*}{dx\,dM_\infty}$$

and the term in the brackets is typically of O(1) for a flat plate. So the Newton-Raphson procedure becomes

$$X_{i+1} = X_i - \frac{G\tan^{-1}\left(\frac{\sqrt{X_i^2-1}}{G}\right) - \tan^{-1}\sqrt{X_i^2-1} + \phi - \nu_0}{\frac{X_i}{\sqrt{X_i^2-1}}\left(\frac{1}{1+\frac{X_i^2-1}{G^2}} - \frac{1}{X_i^2}\right)} \qquad \text{(B7)}$$

APPENDIX C

C.1 Numerical integrations of $\bar{\delta}^{*''}_{g}$

Since the iterations on each j station begin only at a point which is one step downstream of the beginning of the strong interaction, j at that stage is usually larger than 4, typically 50 (allowing the development of a weak interaction over 49 stations before triggering the strong interaction). Hence the integration of $\bar{\delta}^{*''}_{g}$ employs an inversion of the f basic formula for the second derivative, using a back scheme, namely

$$\left.\frac{d^2H}{dX^2}\right|_j = \frac{3H'_j - 4H'_{j-1} + H'_{j-2}}{2(\Delta X)} + O\left[(\Delta X)^2\right] \qquad \text{(C1-1)}$$

Based on this we have

$$\bar{\delta}^{*'}_j = \frac{1}{3}\left\{2\left[(\Delta X)\bar{\delta}^{*''}_j + 2\bar{\delta}^{*'}_{j-1}\right] - \bar{\delta}^{*'}_{j-2}\right\} \qquad \text{(C1-2)}$$

$$\bar{\delta}^{*}_j = \frac{1}{9}\left\{2(\Delta X)\left[2\left(\Delta X\,\bar{\delta}^{*''}_j + 2\bar{\delta}^{*'}_{j-1}\right) - \bar{\delta}^{*'}_{j-2}\right] + 3\left(4\bar{\delta}^{*}_{j-1} - \bar{\delta}^{*}_{j-2}\right)\right\} \qquad \text{(C1-3)}$$

These formulae, when applied for the first two times, use the incompressible weak interaction values for $\bar{\delta}^*$ and $\bar{\delta}^{*'}$, namely

$$\bar{\delta}^* = 1.7208\sqrt{\frac{\nu_0 X}{u_0}}, \qquad \bar{\delta}^{*'} = \frac{0.8604}{\sqrt{Re_x}}$$

where

$$Re_x = \frac{\rho_0 u_0 X}{\mu_0}$$

C.2 Second derivative of $\bar{\delta}^*_c$

Special care must be exercised when numerically differentiating a variable, since differentiation tends to introduce instabilities. It was found that the best formula for $\bar{\delta}^{*\prime\prime}_{c_j}$ is a simple backward scheme, namely

$$\bar{\delta}^{*\prime\prime}_{c_j} = \frac{\bar{\delta}^*_{c_j} - 2\bar{\delta}^*_{c_{j-1}} + \bar{\delta}^*_{c_{j-2}}}{(\Delta \bar{x})^2} \tag{C2-1}$$

C.3 Newton-Raphson Procedure for Improving $(\bar{\delta}^{*\prime\prime})_j$

The basis for the convergence of a calculation at each x-wise station is the agreement between the guessed and calculated $\bar{\delta}^{*\prime\prime}$ for that station to within a specified tolerance. Hence the Newton-Raphson procedure is

$$\begin{cases} \left[\bar{\delta}^{*\prime\prime}_{g_j}\right]_2 = \left[\bar{\delta}^{*\prime\prime}_{c_j}\right]_1 \\ \left[\bar{\delta}^{*\prime\prime}_{g_j}\right]_{i+1} = \left[\bar{\delta}^{*\prime\prime}_{g_j}\right]_i - \dfrac{\left[\bar{\delta}^{*\prime\prime}_{g_j}\right]_i - \left[\bar{\delta}^{*\prime\prime}_{c_j}\right]_i}{1 - \dfrac{\left[\bar{\delta}^{*\prime\prime}_{c_j}\right]_i - \left[\bar{\delta}^{*\prime\prime}_{c_j}\right]_{i-1}}{\left[\bar{\delta}^{*\prime\prime}_{g_j}\right]_i - \left[\bar{\delta}^{*\prime\prime}_{g_j}\right]_{i-1}}}, \quad i \geq 2 \end{cases} \tag{C3-1}$$

where j stands for any x-wise station and c means a computed value.

C.4 Newton-Raphson procedure for improving $(\bar{\delta}^{*''})_{j_{x_{sh}}}$

The basis for obtaining a successively better guess for $\bar{\delta}^{*''}_{j_{x_{sh}}}$ is picking that branch which will result in the correct downstream pressure with negligible pressure gradient. Hence the Newton-Raphson procedure is

$$\left(\bar{\delta}^{*''}_{g_{x_{sh}}}\right)_{i+1} = \left(\bar{\delta}^{*''}_{g_{x_{sh}}}\right)_i - \left\{P\left[\left(\bar{\delta}^{*''}_{g_{x_{sh}}}\right)_i\right] - P_f\right\} \frac{\left(\bar{\delta}^{*''}_{g_{x_{sh}}}\right)_i - \left(\bar{\delta}^{*''}_{g_{x_{sh}}}\right)_{i-1}}{P\left[\left(\bar{\delta}^{*''}_{g_{x_{sh}}}\right)_i\right] - P\left[\left(\bar{\delta}^{*''}_{g_{x_{sh}}}\right)_{i-1}\right]} \tag{C4-1}$$

where P_f is the inviscid downstream pressure (see Appendix D) and $P[(\bar{\delta}^{*''}_{g_{x_{sh}}})_j]$ is the pressure at the downstream station, as calculated using the jth guess for $\bar{\delta}^{*''}_{x_{sh}}$. The starting values used in the program are:

$$\left(\bar{\delta}^{*''}_{g_{x_{sh}}}\right)_1 = \hat{K}_1 \left[\bar{\delta}^{*''}_{g_{x_{sh}-1}}\right] \qquad \text{with } \hat{K}_1 = -0.1$$

$$\left(\bar{\delta}^{*''}_{g_{x_{sh}}}\right)_2 = \hat{K}_2 \left(\bar{\delta}^{*''}_{g_{x_{sh}}}\right)_1 \qquad \text{with } \hat{K}_2 = 1.5$$

APPENDIX D

FIRST GUESSES FOR $\delta^{*''}_{j_{x_{sh}}}$ and x_o

Since the downstream boundary condition demonstrates a nodal-type of behavior, extremely small changes in $(\delta^{*''})_{g_{j_{x_{sh}}}}$ produce large changes in the branching solutions. Hence the first guess for $\delta^{*''}_{j_{x_{sh}}}$ is important in order to start a branching solution. A good initial guess enables the employment of small corrections to it as an effective control parameter. For incompressible flow over a flat plate,

$$\delta^* = 1.7208\sqrt{\frac{\nu_\infty x}{u_\infty}} \tag{D1}$$

from which

$$\delta^{*''} = -0.4302\sqrt{\frac{\nu_\infty}{u_\infty x^3}} \tag{D2}$$

and

$$\delta^{*''}_{x_{sh}} = -0.4302\sqrt{\frac{\nu_o}{u_o x^3_{sh}}} \tag{D3}$$

In nondimensional form this becomes

$$\frac{d^2\bar{\delta}}{d\bar{x}^2} \quad {}^{2}e_{x_o} x_o \delta^{*''} \tag{D4}$$

giving as the first guess

$$\left[\frac{d^2\bar{\delta}^*}{dX^2}\right]_{X_{sh}} = -0.4302\left(Re_{X_{sh}}\right)^{3/2}\left(\frac{X_o}{X_{sh}}\right)^3 \tag{D5}$$

The first guess for x_o is based on Rose's empirical formula (Ref. 16):

$$\frac{X_o}{X_{sh}} = 1 - 68.5\frac{(P_f-1)^{0.73}\left(\frac{X_o}{X_{sh}}\right)}{M_o^{2.4}\,Re_{X_o}^{0.25}} \tag{D6}$$

This equation is iterated upon until a converged value for $\frac{x_o}{x_{sh}}$ is obtained. Here x_{sh} is the point where the idealized shock impinges on the boundary layer, and P_{final} is determined from inviscid considerations:

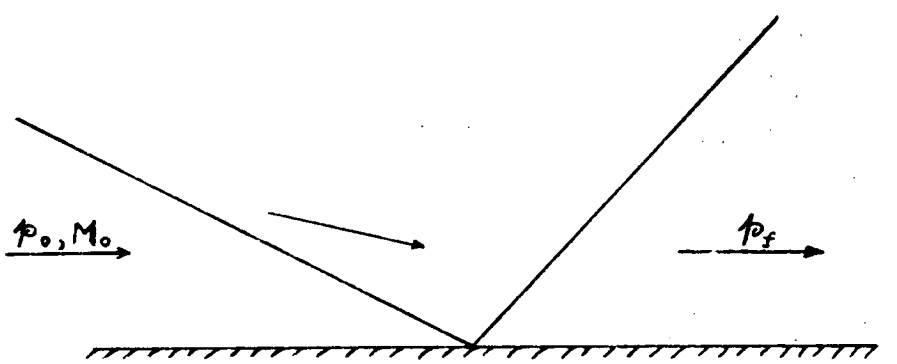

$$P_f = \frac{p_f}{p_o}$$

APPENDIX E

PROCEDURE FOR THE x_o ITERATION

The following method is employed for the successive improvement of x_o:

$$(X_o)_{i+1} = (X_o)_i \cdot (K_1)_i \tag{E1}$$

or

$$(X_o)_{i+1} = (X_o)_i \cdot (K_2)_i \tag{E2}$$

where $K_1 < 1$ to produce a smaller x_o and thereby a more compressive branch, and $K_2 > 1$ to produce a larger x_o and thus a less compressive branch. Once a correction has been done on x_o, the K's are updated as follows:

$$(K_1)_{i+1} = \frac{1}{2}\left[1 + (K_2)_i^{-1}\right] \qquad (K_1)_1 = 0.95 \tag{E3}$$

$$(K_2)_{i+1} = 2\left[1 + (K_1)_i\right]^{-1} \qquad (K_2)_1 = 1/0.95 \tag{E4}$$

One of these new K's is used in the next x_o-iteration to produce a corrected either more expansive or more compressive branch, as necessary, until the right branch is found. This iteration is performed in conjunction with the $(\bar{\delta}^{*''})_{j_{x_{sh}}}$ iteration, explained in Appendix C4.

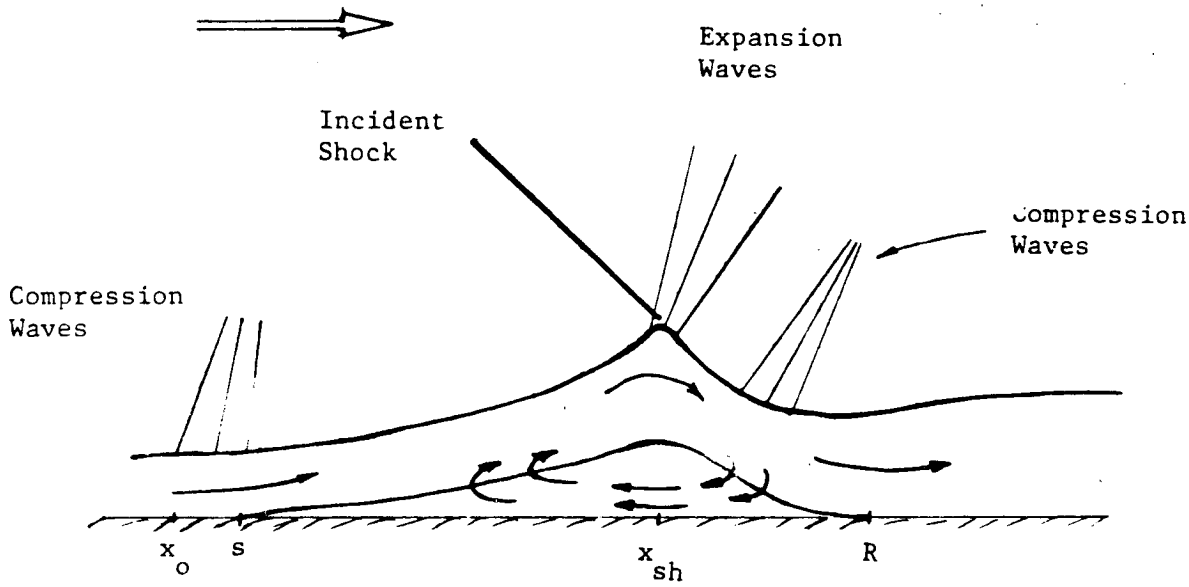

Fig. 1 Oblique shock-laminar boundary layer interaction on a flat plate, showing separated region.

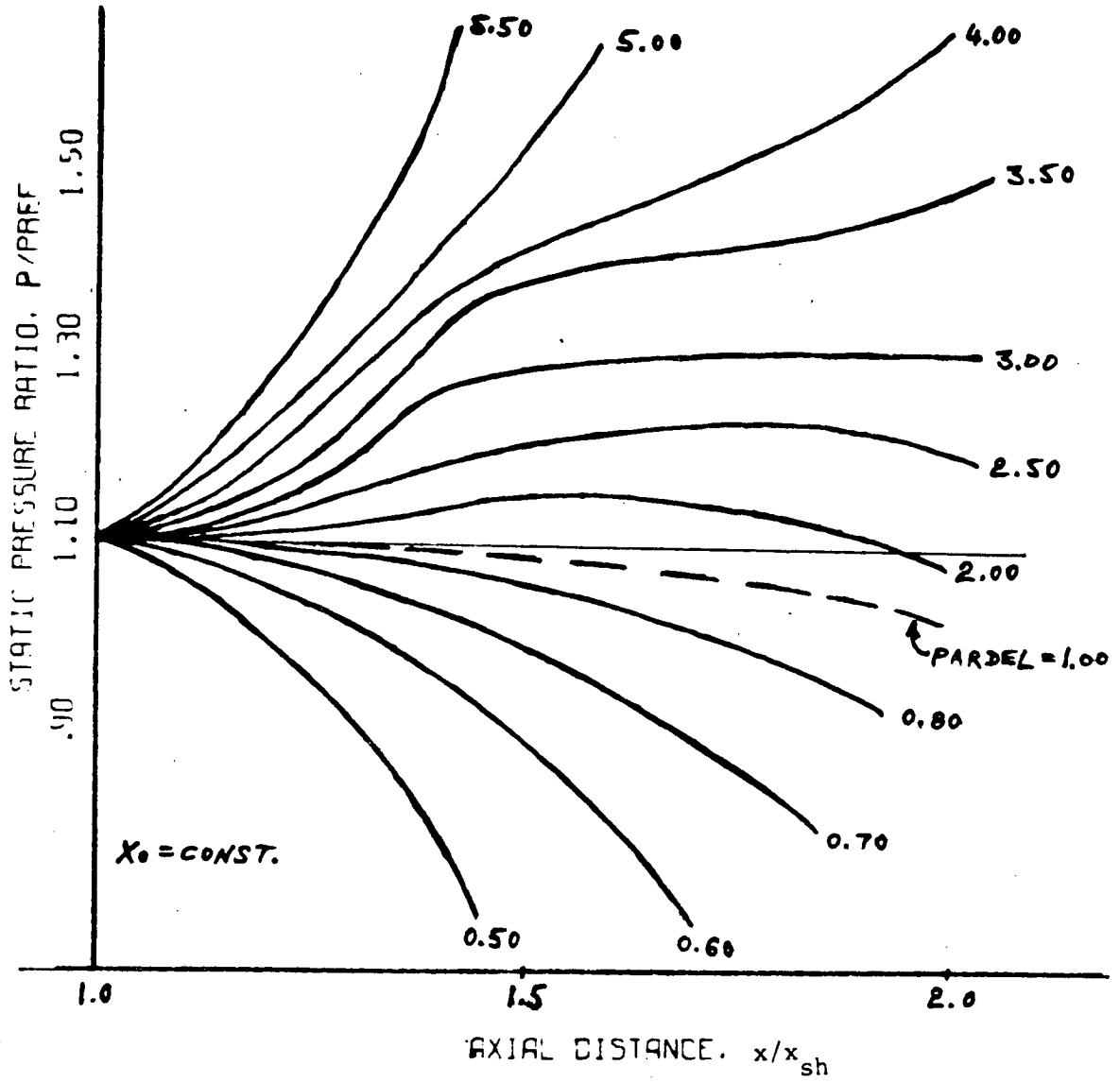

Fig. 2 Influence of branch control parameter, Pardel, on branching behavior.

$$\left(\text{Pardel} = \left[\left(\frac{d^2\bar{\delta}^*}{dX^2}\right)_{x_{sh}}\right]_{\substack{\text{strong}\\ \text{interaction}}} \Big/ \left[\left(\frac{d^2\bar{\delta}^*}{dX^2}\right)_{x_{sh}}\right]_{\substack{\text{weak}\\ \text{interaction}}}\right)$$

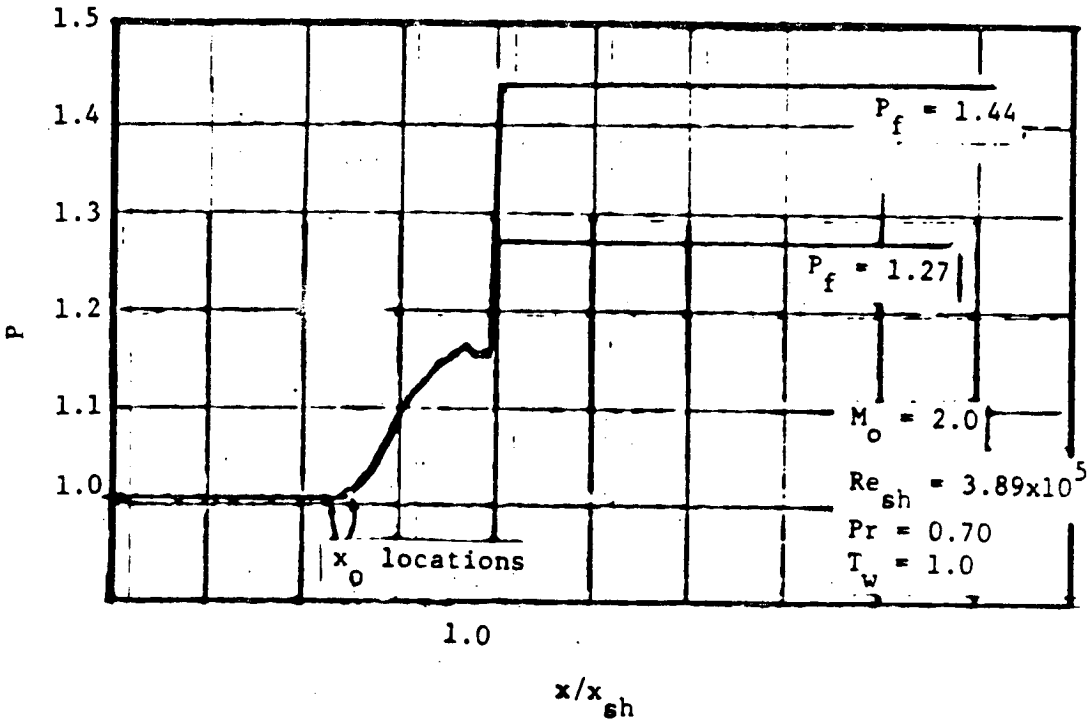

Fig. 3 Effect of changing the location of the start of the strong interaction, x_o, with fixed location of shock impingement.

Fig. 4 Flowchart for computer program

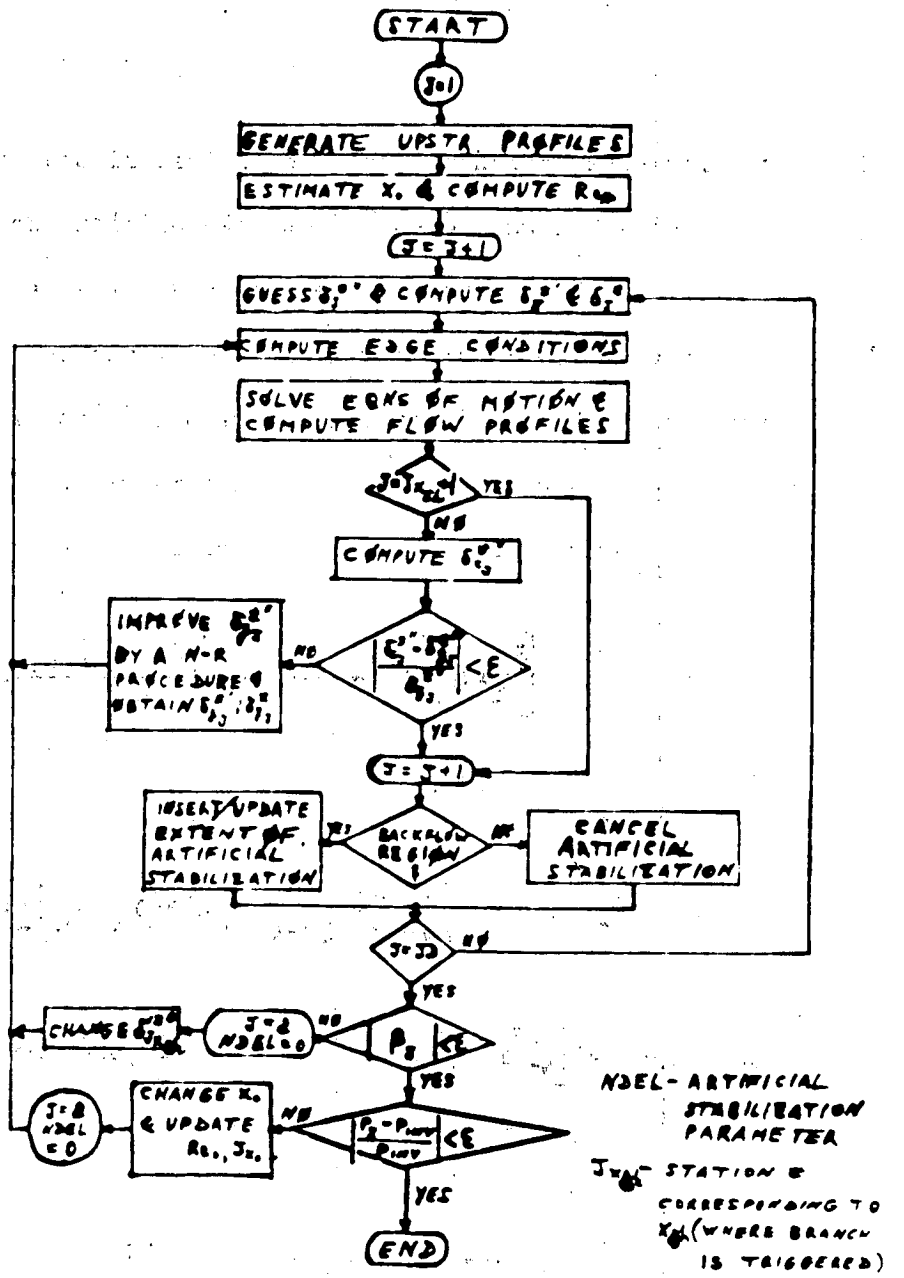

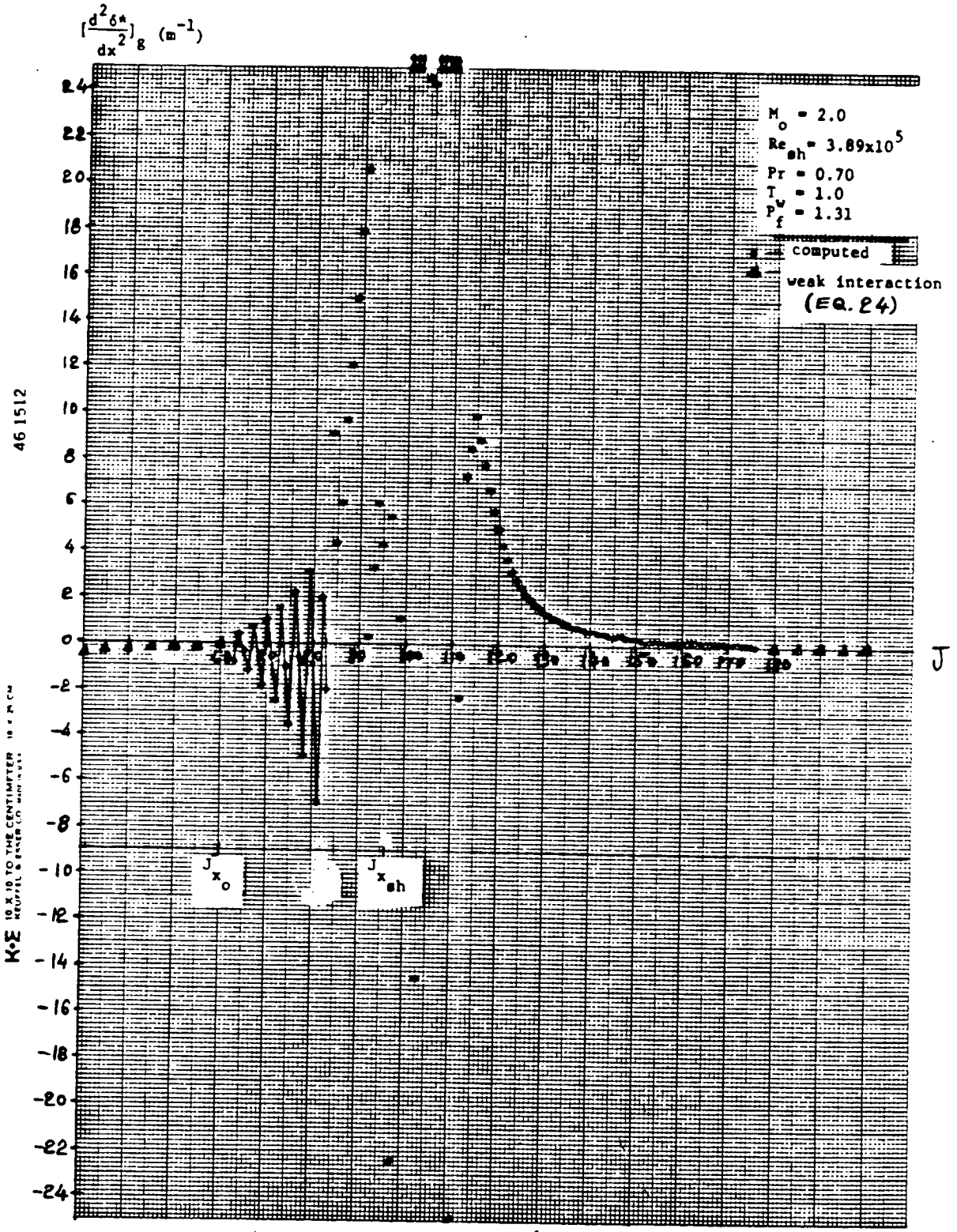

Fig. 5 Variation of δ^*_g" with streamwise station.

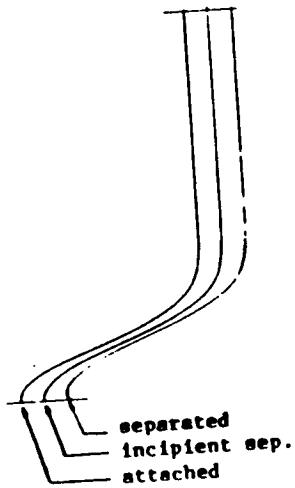

Fig. 6a Streamwise velocity profiles in separation region

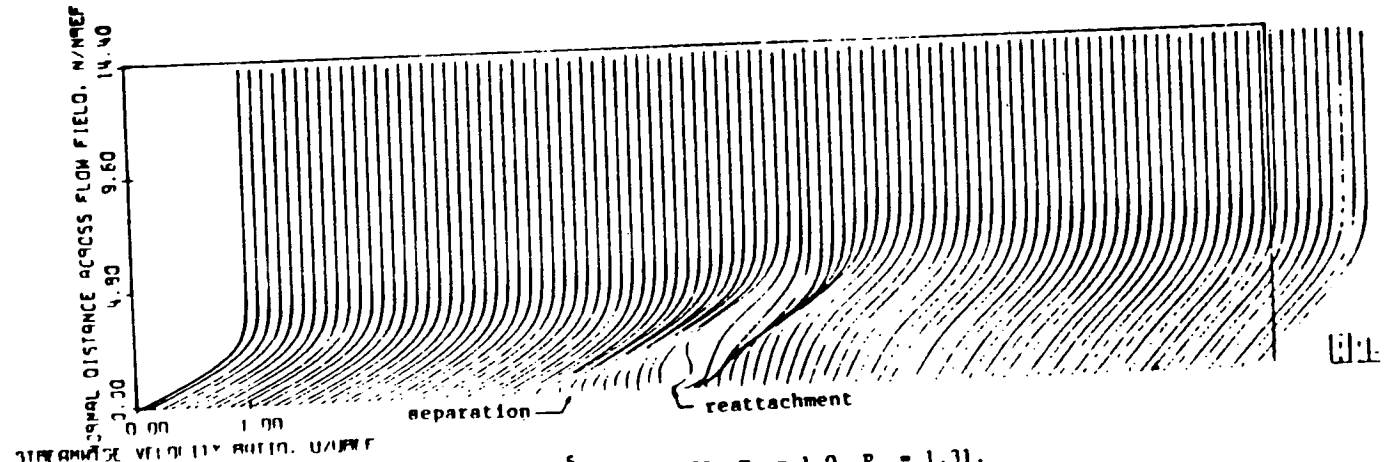

Fig. 6 $M_o = 2.0$, $Re_{\theta h} = 3.89 \times 10^5$, $Pr = 0.70$, $T_w = 1.0$, $P_f = 1.31$.

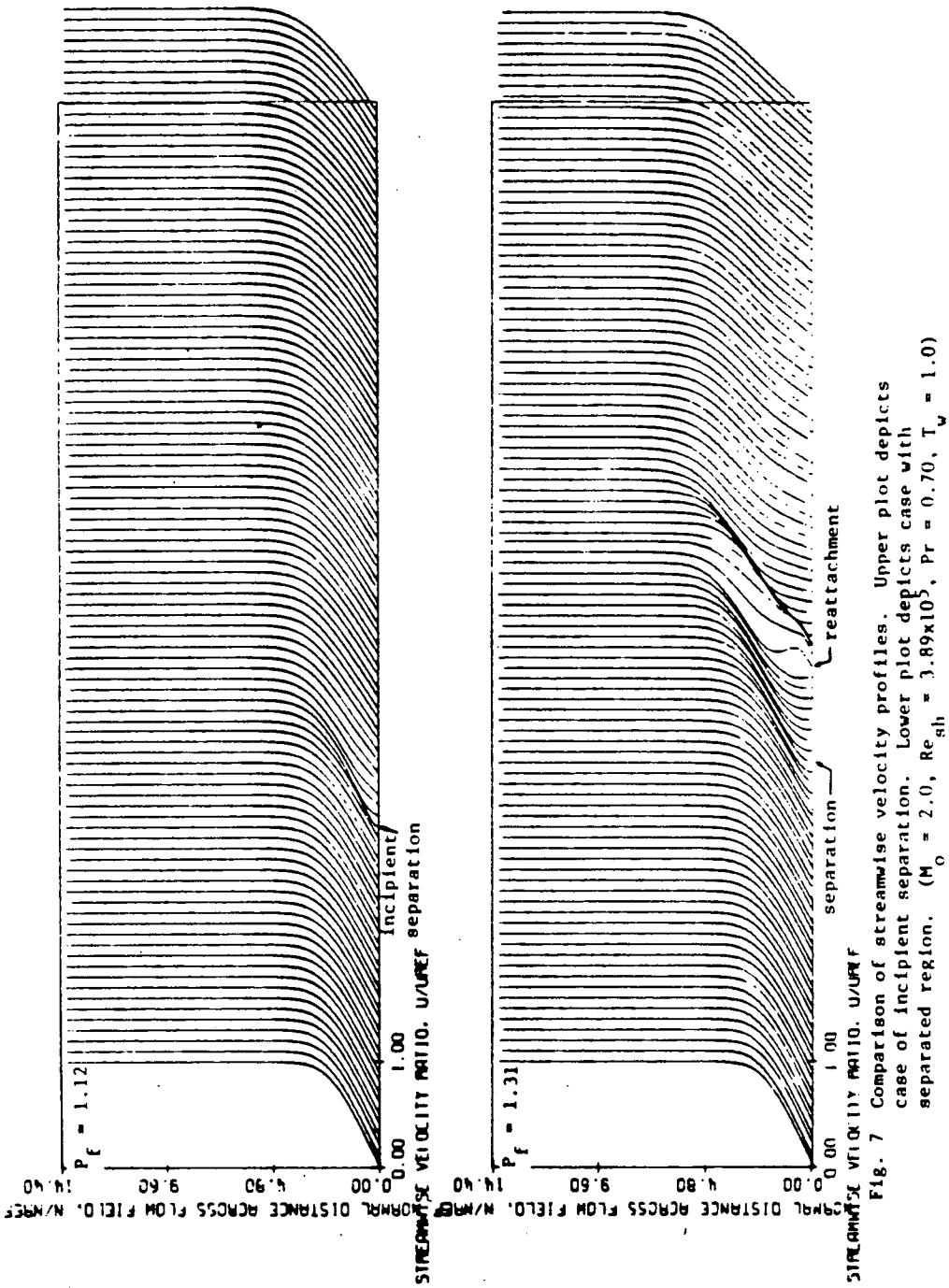

Fig. 7 Comparison of streamwise velocity profiles. Upper plot depicts case of incipient separation. Lower plot depicts case with separated region. (M_o = 2.0, Re_{sh} = 3.89x10^5, Pr = 0.70, T_w = 1.0)

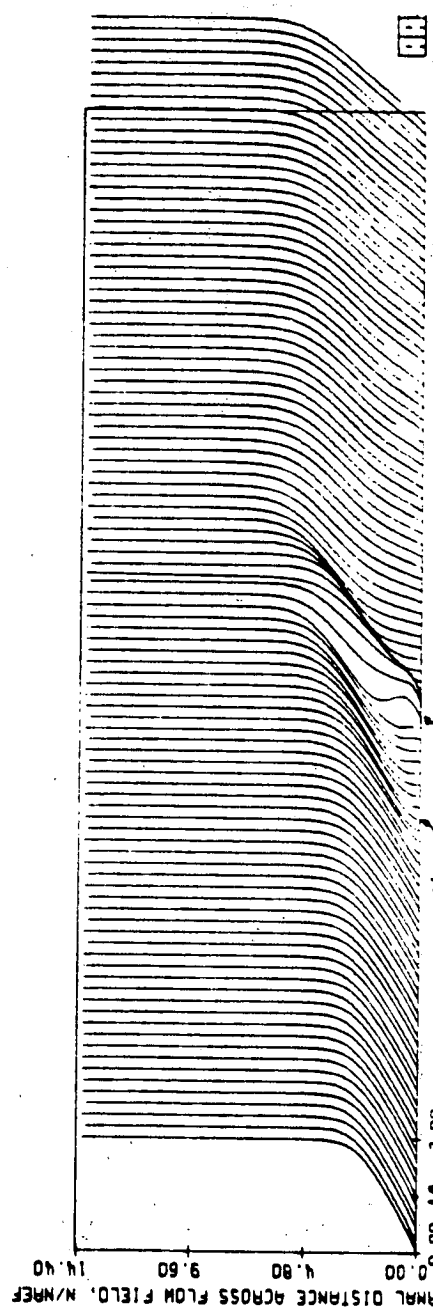

Fig. 8 $M_o = 2.0$, $Re_{sh} = 3.89 \times 10^5$, $Pr = 0.70$, $T_w = 1.0$, $P_f = 1.31$

$$N/NREF = \frac{1}{x_o}\sqrt{Re_{x_o}}$$

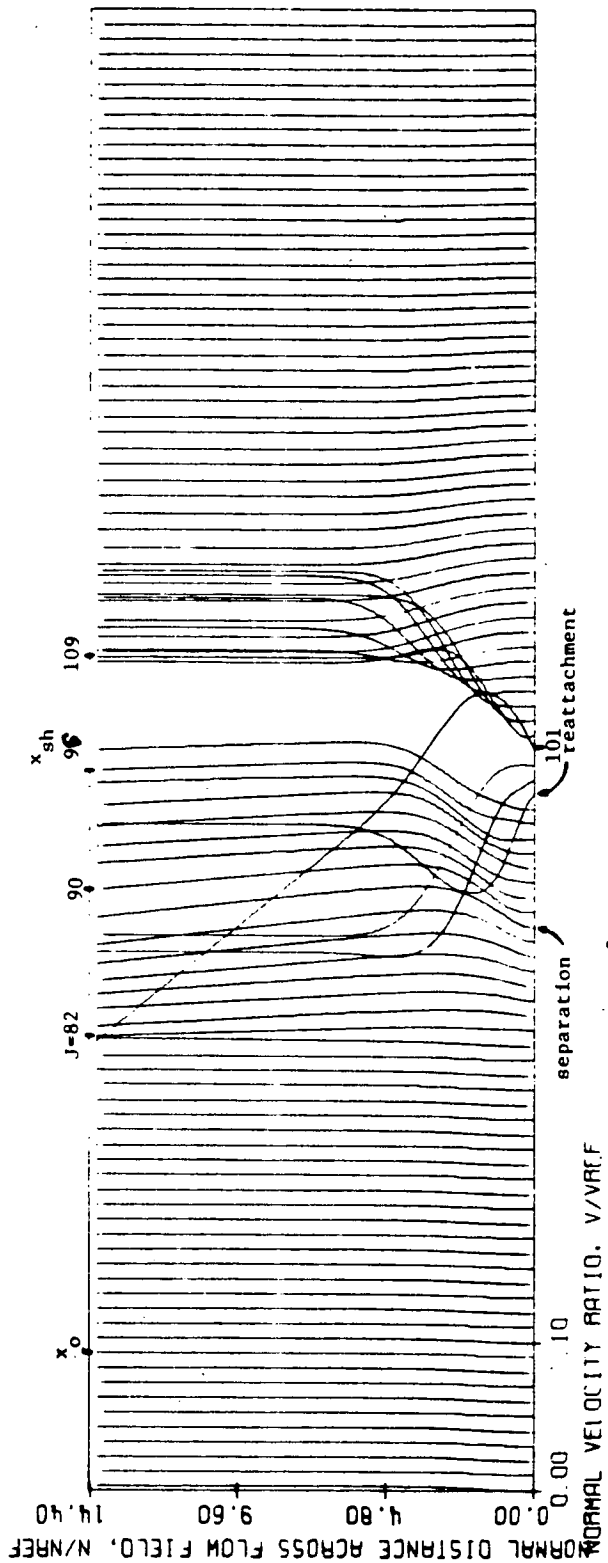

Fig. 9 $M_o = 2.0$, $Re_{sh} = 3.89 \times 10^5$, $Pr = 0.70$, $T_w = 1.0$, $P_f = 1.31$

$$N/NREF = \frac{y}{x_o}\sqrt{Re_{x_o}}$$

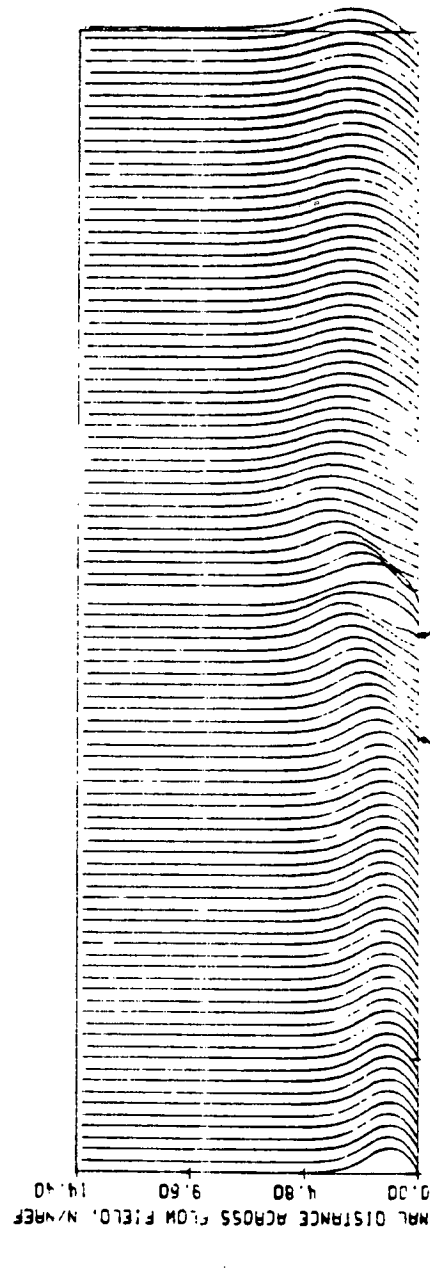

Fig. 10 $M_o = 2.0$, $Re_{sh} = 3.89 \times 10^5$, $Pr = 0.70$, $T_w = 1.0$, $P_r = 1.31$

$$N/NREF = \frac{Y}{x_o}\sqrt{Re_{x_o}}$$

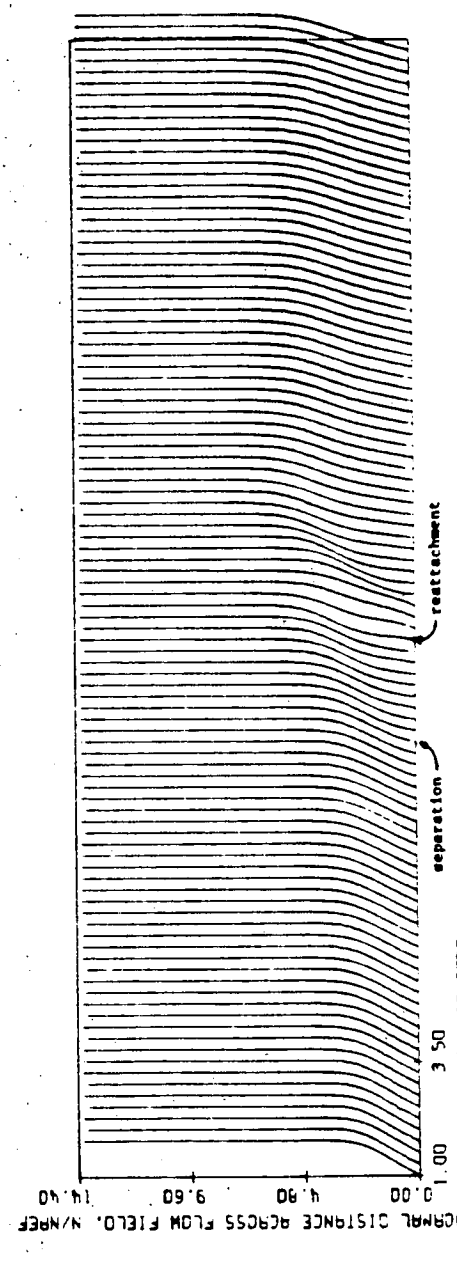
NORMAL DISTANCE ACROSS FLOW FIELD, N/NREF
0.00
4.80
9.60
14.40
1.00
3.50
separation
reattachment
TOTAL TEMPERATURE RATIO, TS/TREF
Fig. 11 M_o = 2.0, Re_{sh} = 3.89x10^5, Pr = .70, T_w = 1.0, P_f = 1.31
$N/NREF = \frac{Y}{x_o}\sqrt{Re_{x_o}}$

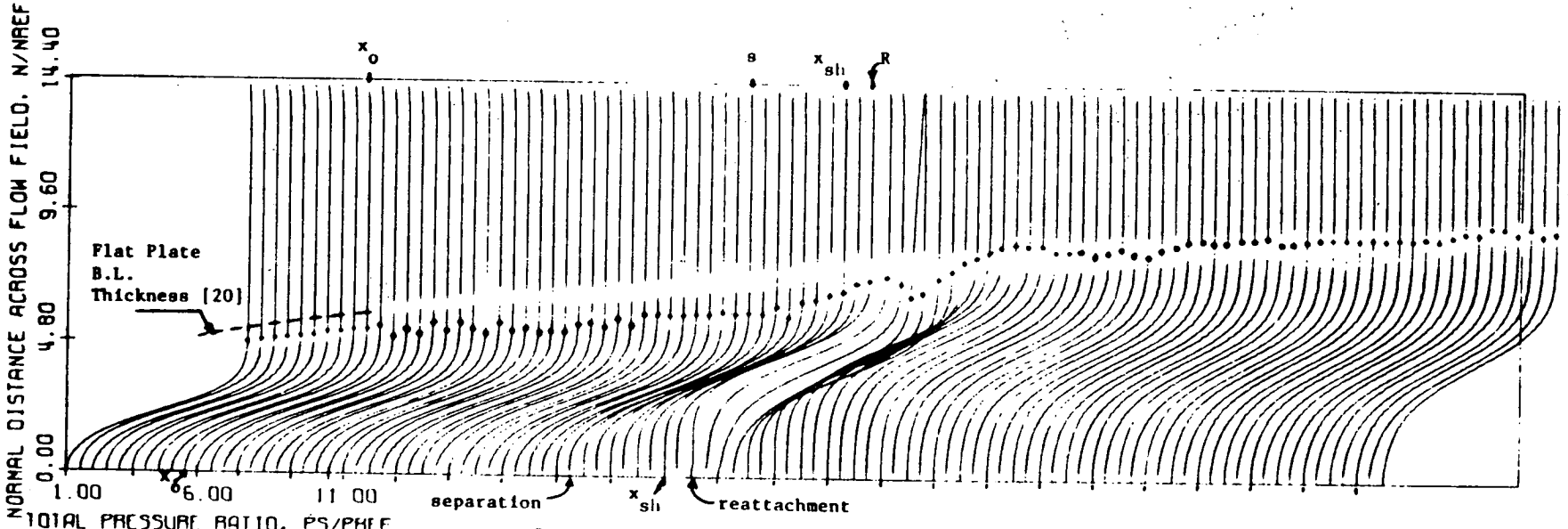

Fig. 12 $M_o = 2.0$, $Re_{sh} = 3.89 \times 10^5$, $Pr = 0.70$, $T_w = 1.0$, $P_f = 1.31$

$$N/NREF = \frac{y}{x_o}\sqrt{Re_{x_o}}$$

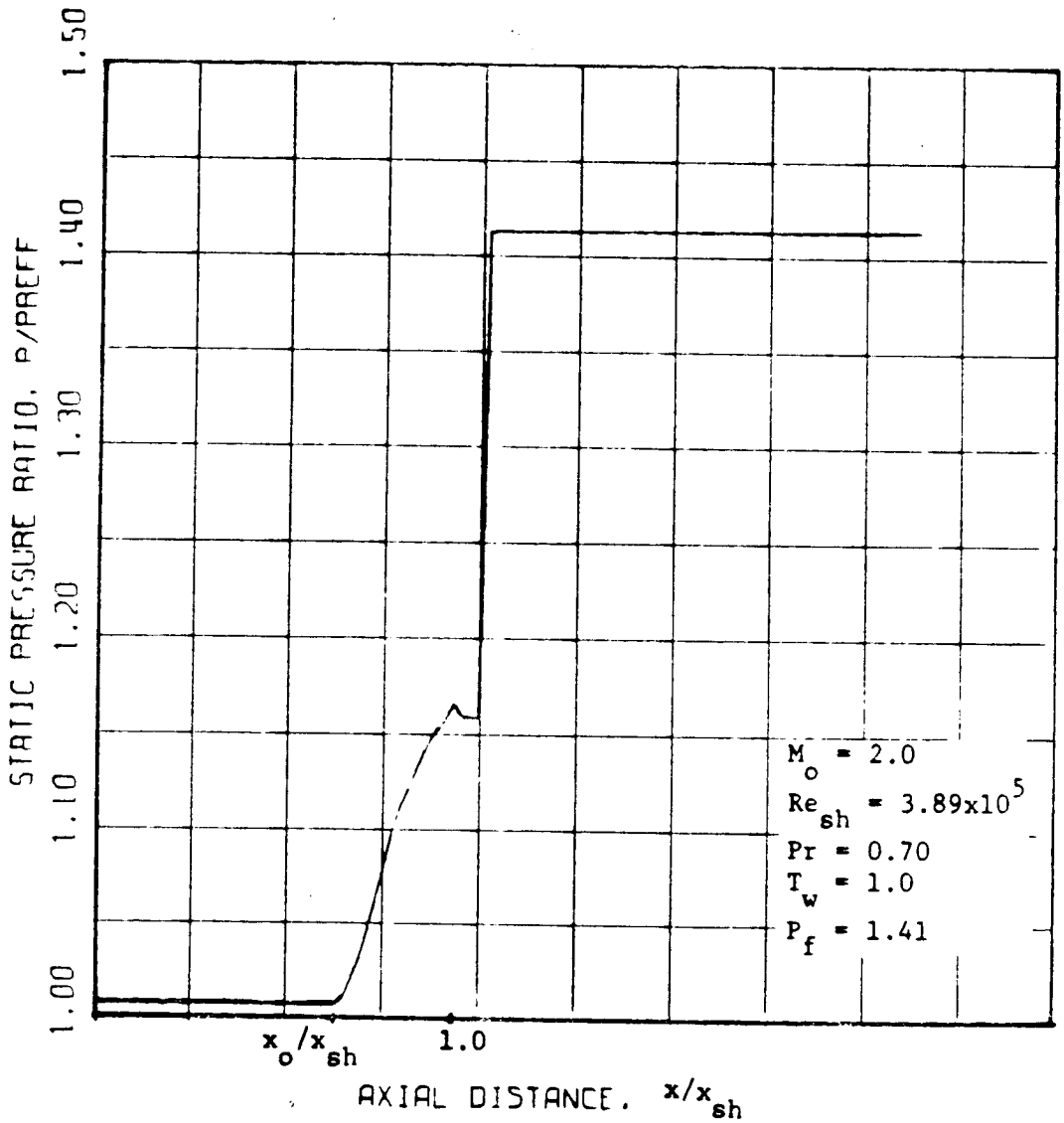

Fig. 13 Typical static pressure profile.

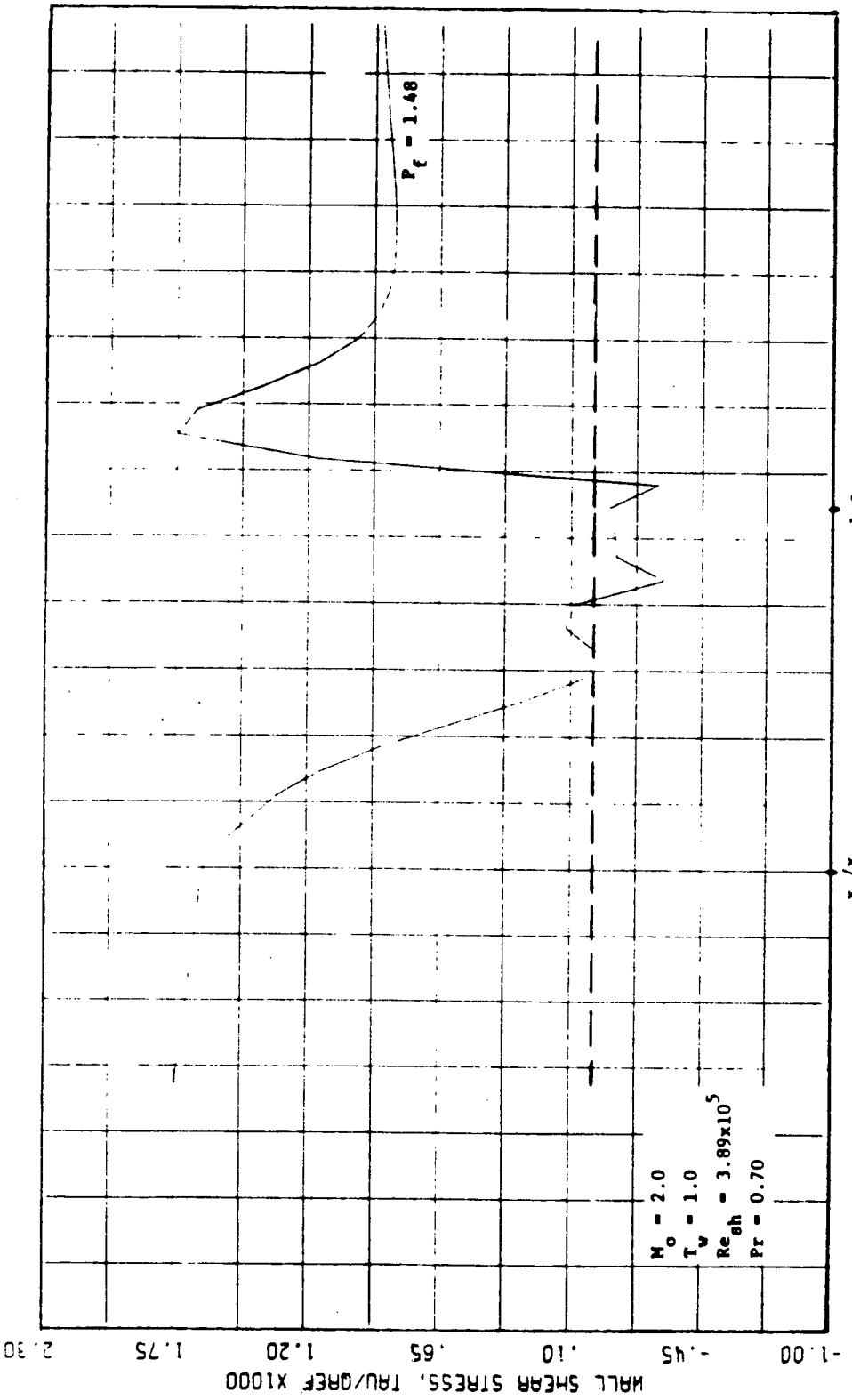

Fig. 14 Typical C_f profile as produced by program.

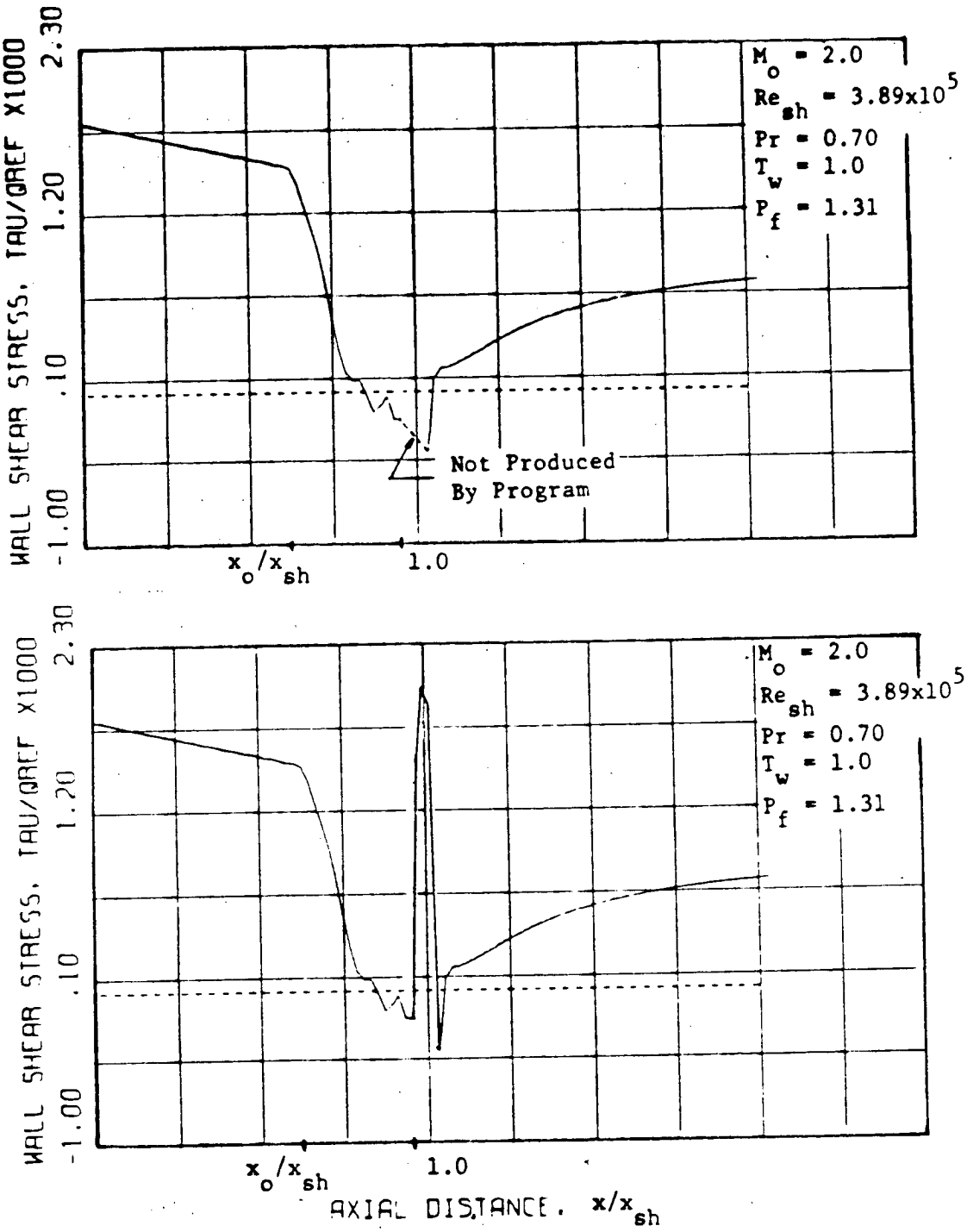

Fig. 15 Original and "corrected" skin friction for P_f = 1.31.

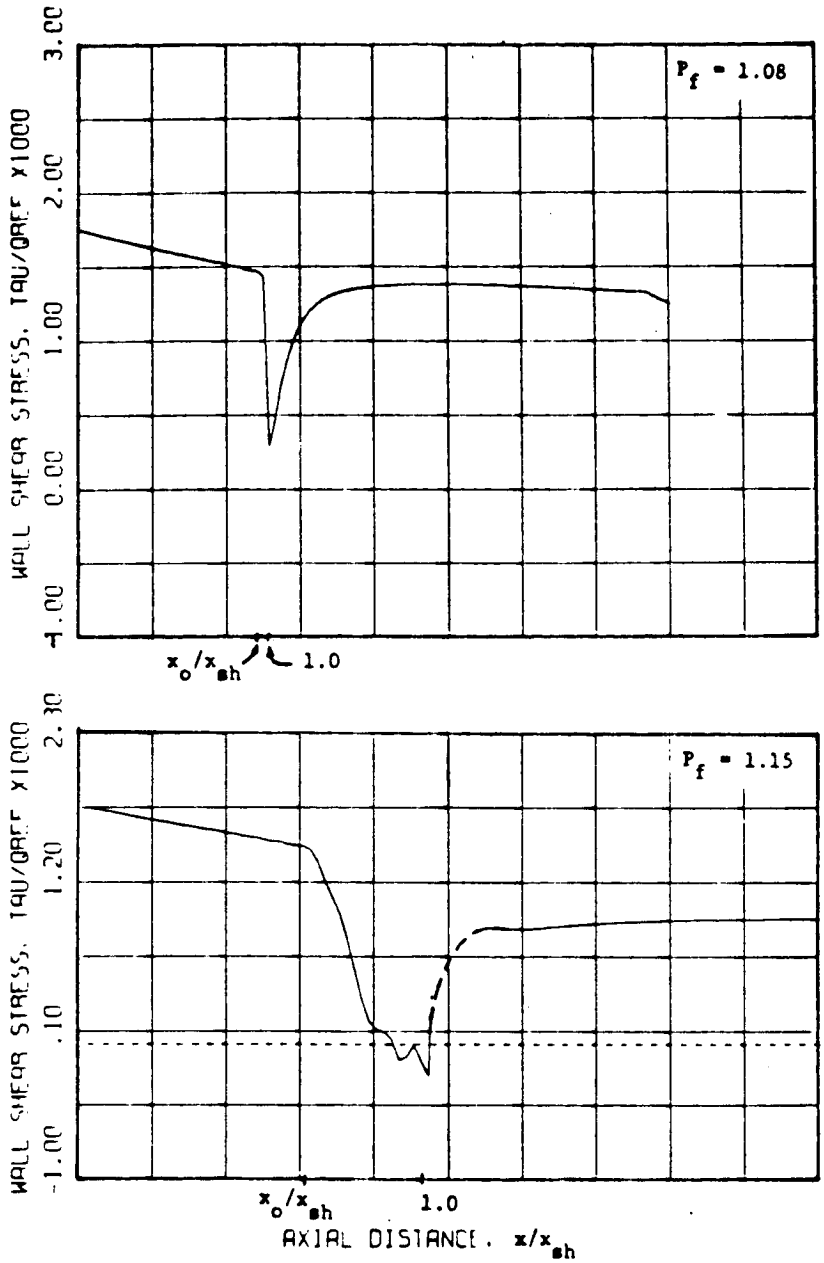

Fig. 16 Comparison between skin friction plots. Upper plot depicts case approaching incipient separation. Lower plot depicts case with small separated region. (M_{sh} = 2.0, Re_{sh} = 3.89×10^5, Pr = 0.70, T_w = 1.0, dashed line not produced by program.)

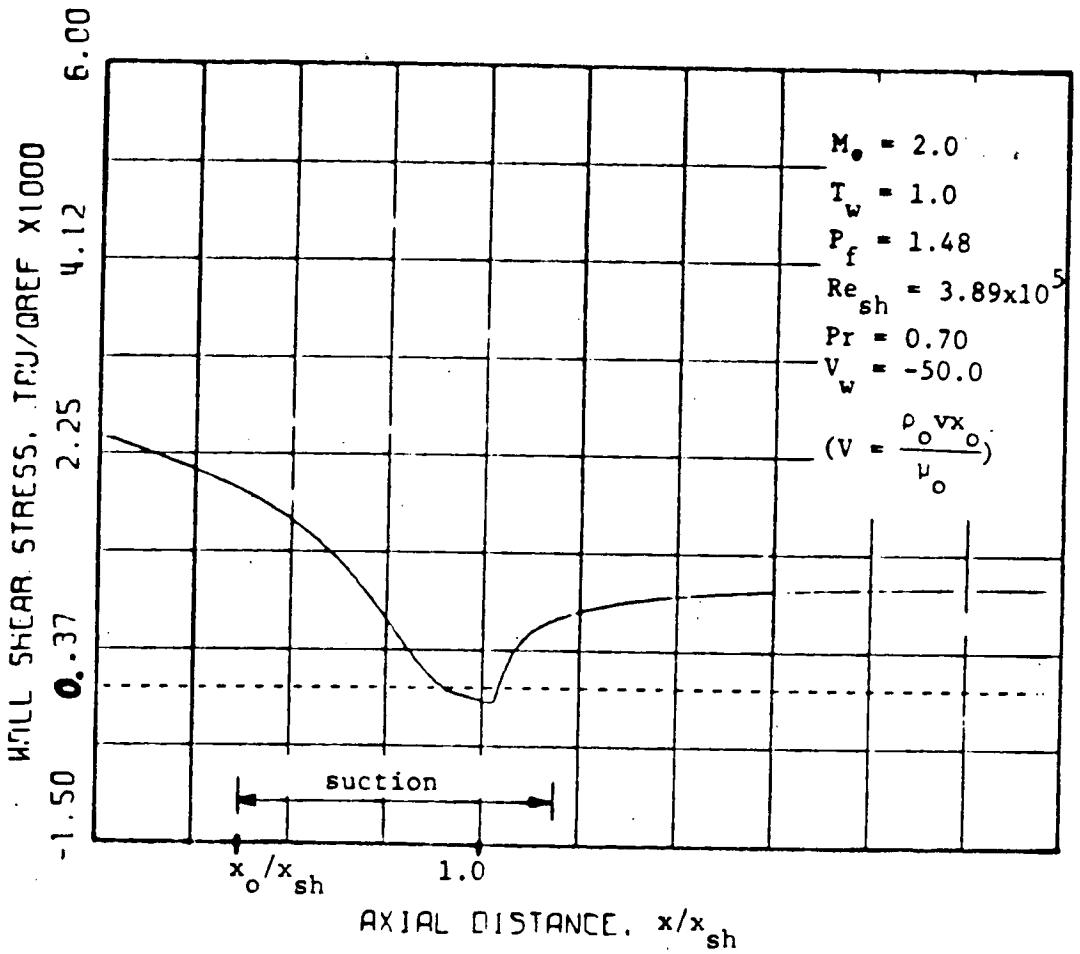

Fig. 17 Effect of suction on C_f profile.

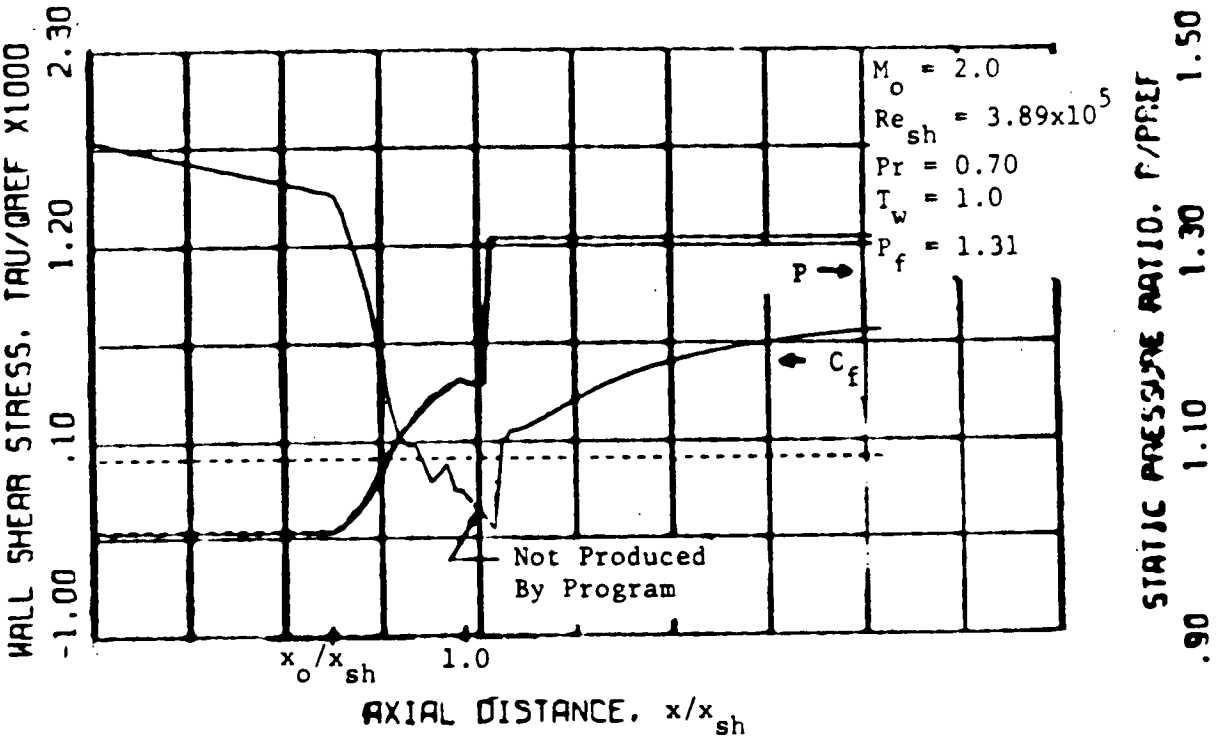

Fig. 18 C_f and P profiles for P_f = 1.31

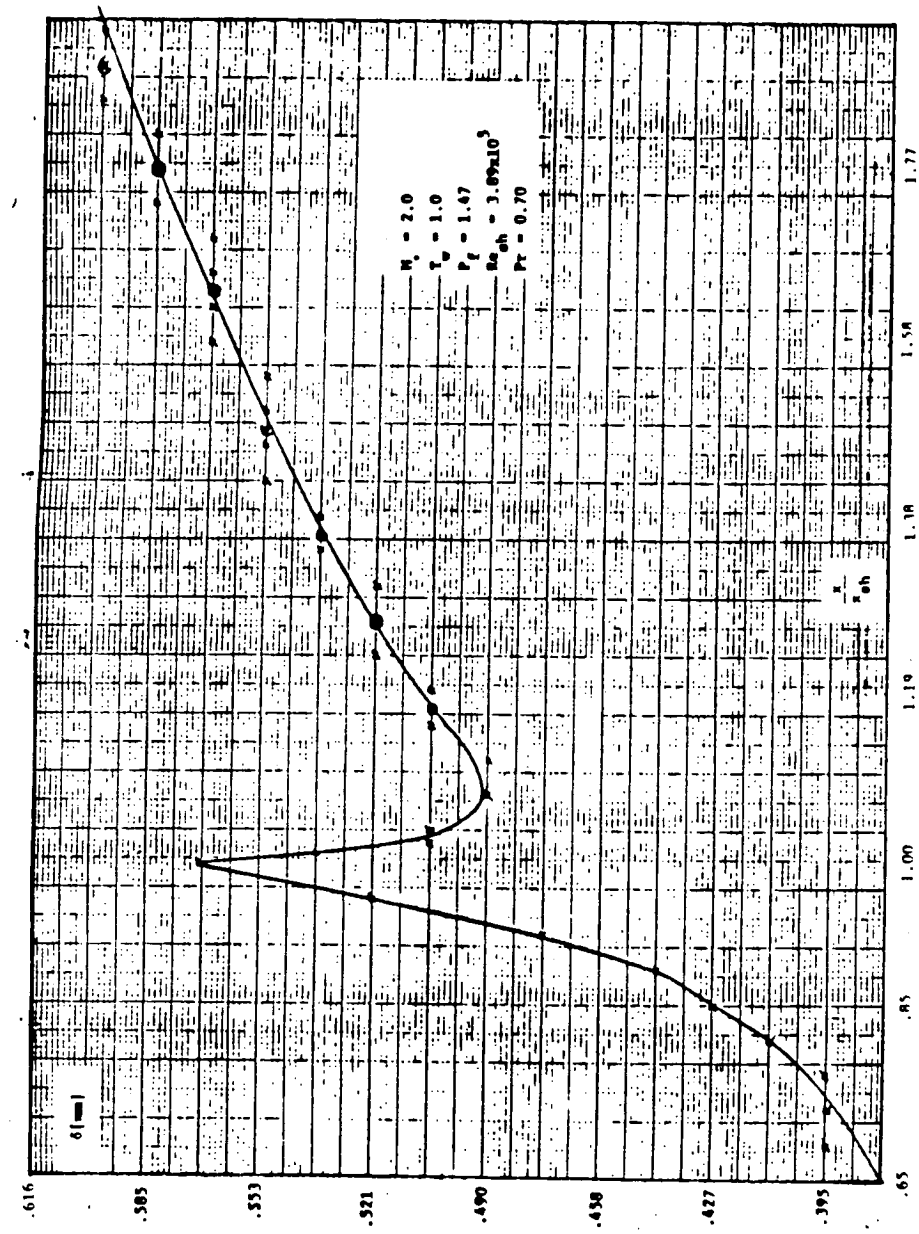

Fig. 19 Streamwise distribution of boundary layer thickness.

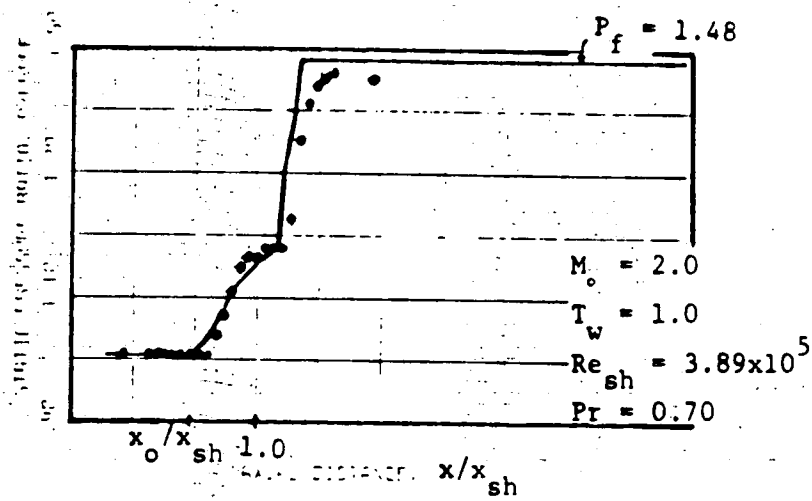

Fig. 20 Comparison between experiment and theory. Experimental points are from Hakkinen, Greber, Trilling and Abarbanel [4]. (M_o = 2.0, Re_{sh} = 4.02x10^5, Pr = 0.72, $p_f p_o$ = 1.47, Sutherland Law, T_{st}^* = 295°K, s* = 110°K).

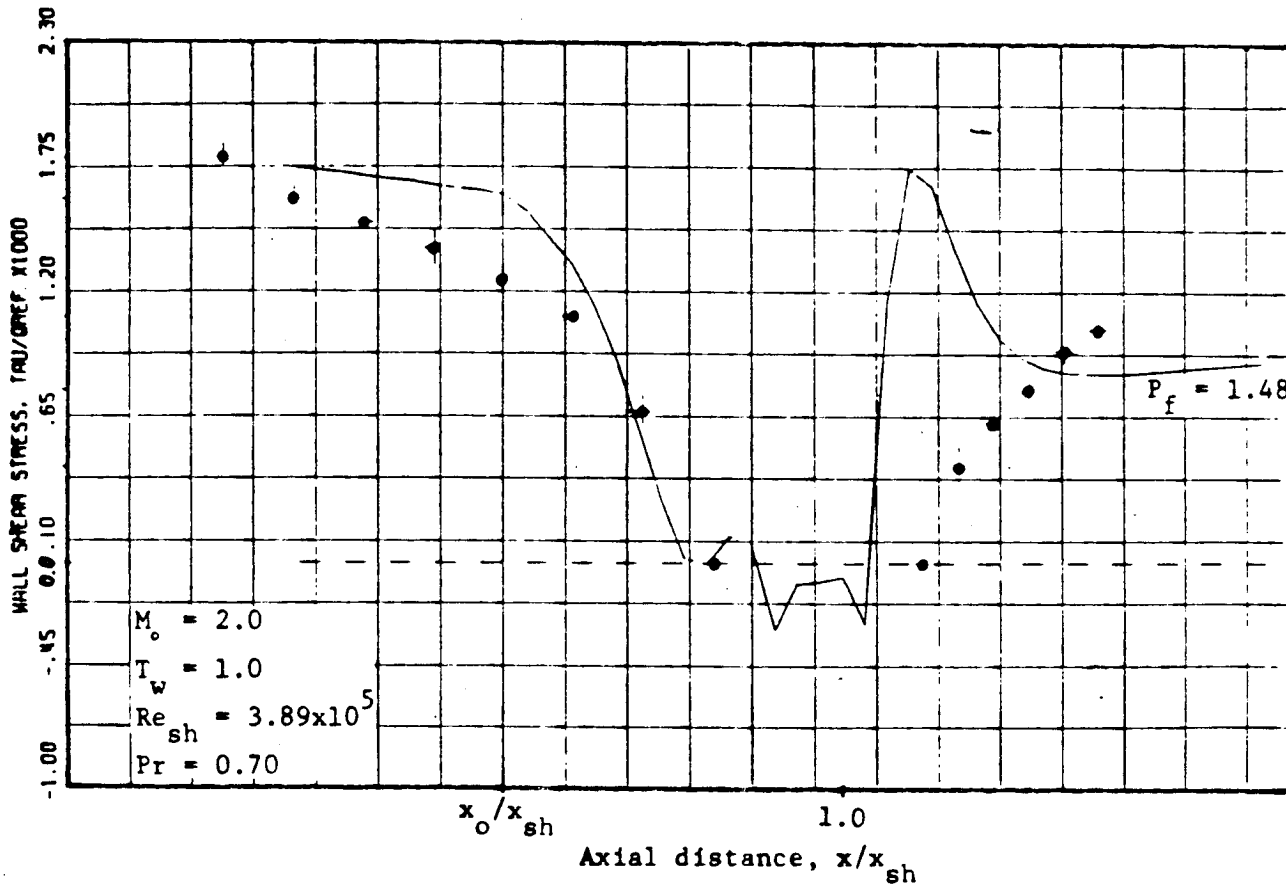

Fig. 21 Comparison between experiment and theory. Experimental points are from Hakkinen, Greber, Trilling and Abarbanel [4]. (M_o = 2.0, Re_{sh} = 4.02 x 10^5, Pr = 0.72, p_f/p_o = 1.47, Sutherland Law, T_{st}^* = 295°K, s^* = 110°K).

1. Report No.	2. Government Accession No.	3. Recipient's Catalog No.
NASA CR-159829		

4. Title and Subtitle	5. Report Date
CALCULATION OF OBLIQUE-SHOCK-WAVE LAMINAR-BOUNDARY-LAYER INTERACTION ON A FLAT PLATE	March 1980
	6. Performing Organization Code

7. Author(s)	8. Performing Organization Report No.
Uriel Goldberg, General Electric Co., Lynn, Mass., Eli Reshotko, Case Western Reserve University, Cleveland, Ohio	None
	10. Work Unit No.

9. Performing Organization Name and Address	11. Contract or Grant No.
Case Western Reserve University Cleveland, Ohio 44106	NGR-36-027-064
	13. Type of Report and Period Covered
12. Sponsoring Agency Name and Address	Contractor Report
National Aeronautics and Space Administration Washington, D.C. 20546	14. Sponsoring Agency Code

15. Supplementary Notes

Final report. Project Manager, Allan R. Bishop, Propulsion Systems Division, NASA Lewis Research Center, Cleveland, Ohio 44135.

16. Abstract

A finite-difference solution to the problem of the interaction between an impinging oblique shock wave and the laminar boundary layer on a flat plate is presented. The boundary layer equations coupled with the Prandtl-Meyer relation for the external flow are used to calculate the flow field. An improved method for the calculation of the separated flow region is presented and discussed. Comparasions between this theory and the experimental results of Hakkinen, Greber, Trilling and Abarbanel show fairly good agreement. Results are presented for the case of a cooled wall with an oncoming flow at Mach number 2.0 without and with suction. The results show that a small amount of suction greatly reduces the extent of the separated region in the vicinity of the shock impingement location.

17. Key Words (Suggested by Author(s))	18. Distribution Statement
Boundary-layer Separation Shock wave Strong interaction	Unclassified - unlimited STAR Category 34

19. Security Classif. (of this report)	20. Security Classif. (of this page)	21. No. of Pages	22. Price*
Unclassified	Unclassified	87	

* For sale by the National Technical Information Service, Springfield, Virginia 22161